Mergers of Black Hole – Neutron Star binaries. I. Methods and First Results

Emmanouela Rantsiou[1], Shiho Kobayashi[2], Pablo Laguna[3] and Frederic Rasio[1]

ABSTRACT

We use a 3-D relativistic SPH (Smoothed Particle Hydrodynamics) code to study mergers of black hole – neutron star (BH–NS) binary systems with low mass ratios, adopting $M_{NS}/M_{BH} \simeq 0.1$ as a representative case. The outcome of such mergers depends sensitively on both the magnitude of the BH spin and its obliquity (i.e., the inclination of the binary orbit with respect to the equatorial plane of the BH). In particular, only systems with sufficiently high BH spin parameter a and sufficiently low orbital inclinations allow any NS matter to escape or to form a long-lived disk outside the BH horizon after disruption. Mergers of binaries with orbital inclinations above $\sim 60^o$ lead to complete prompt accretion of the entire NS by the BH, even for the case of an extreme Kerr BH. We find that the formation of a significant disk or torus of NS material around the BH always requires a near-maximal BH spin and a low initial inclination of the NS orbit just prior to merger.

Subject headings: binaries: close — black hole physics — stars: neutron — relativity — gamma rays: bursts

1. Introduction

Over the past two decades, the modelling of double compact objects (DCOs) has attracted special interest among theorists, mainly because such systems are expected to be

[1]Department of Physics and Astronomy, Northwestern University, Evanston, IL 60208, USA.
email: emmanouela@northwestern.edu, rasio@northwestern.edu

[2]Astrophysics Research Institute, Liverpool John Moores University, Twelve Quays House, Egerton Wharf, Birkenhead CH41 1LD.
email: sk@astro.livjm.ac.uk

[3]Department of Astronomy and Astrophysics and Department of Physics, Pennsylvania State University, University Park, PA 16802, USA.
email: pablo@astro.psu.edu

strong sources of gravitational waves (GWs). Their inspiral and merger GW signals cover a wide frequency band, from $\sim 10^{-4} - 10^{-1}\,\mathrm{Hz}$ for supermassive black hole binaries of $\sim 10^4 - 10^7\,M_\odot$ (Arun 2006) to $\sim 1000\,\mathrm{Hz}$ for NS–NS binaries, providing potential sources both for ground-based interferometers (LIGO, VIRGO, etc.) and space-based detectors (LISA). The inspiral signals can provide information on the spins and masses of the compact objects (e.g., Poisson & Will 1995). Moreover the merger signal of BH–NS and NS–NS binaries is believed to carry information on the NS structure and equation of state (EOS) of matter at nuclear densities (Faber & Rasio 2000; Faber et al. 2001; Faber & Rasio 2002). It is interesting to mention here that for BH–NS mergers of massive enough BHs ($M \gtrsim 100\,M_\odot$), where the NS is expected to plunge into the BH as a whole, not much information on the NS EOS will be carried by the GW signal. For BH–NS binaries, only the merger of the NS with a stellar-mass BH will allow for the NS to disrupt outside the BH's innermost stable circular orbit (ISCO; this is emphasized and explained in more detail later on in this paper) and enrich the GW signal with information on the physics of the NS matter.

Even though the GW signals from the inspiral of NS–NS binaries is accessible to ground-based interferometers, covering the frequency range $\sim 40 - 1000\,\mathrm{Hz}$, the signals from their final mergers will probably be lost in the high-frequency noise level (Vallisneri 2000; Faber et al. 2002). On the other hand, the GW merger signals for many BH–NS binaries are expected to lie well within the sensitivity band of LIGO, at frequencies $\sim 100 - 500\,\mathrm{Hz}$.

Although double NS binaries have been observed (Thorsett & Chakrabarty 1999; Burgay et al. 2003), BH–NS and BH–BH binaries remain undetected. Moreover, the few observed NS–NS binaries (binary pulsars with NS companions and one double pulsar) are subject to considerable selection effects. Therefore it is not currently possible to infer much empirically about the general properties of DCOs based on the observed sample. Theorists rely instead on binary evolution and population synthesis models to make predictions about the formation, evolution and properties of such binaries (e.g., Belczynski et al. 2007; Nelemans et al. 2001). These models give estimates of merger rates for DCOs and the corresponding detection rates for the various GW interferometers. NS–NS binaries are expected to merge with rates $\sim 1 - 145\,\mathrm{Myr}^{-1}$ per MWEG (Milky Way Equivalent Galaxy) and the equivalent rate for BH–NS binaries is $\sim 0.07 - 5\,\mathrm{Myr}^{-1}$ per MWEG (Kim et al. 2006; Belczynski et al. 2007). For NS–NS binaries the detection rate estimations are $\sim (0.4 - 60) \times 10^{-3}\,\mathrm{yr}^{-1}$ and $\sim 2 - 330\times\,\mathrm{yr}^{-1}$ for LIGO and Advanced LIGO respectively (Kim et al. 2006), while for BH–NS binaries the equivalent rates are $\sim 3 \times 10^{-3} - 2 \times 10^{-2}\,\mathrm{yr}^{-1}$ and $0.7 - 40\ \mathrm{yr}^{-1}$ (Belczynski et al. 2007). Although the detection rates are quite low for the current LIGO stage, the estimations are very promising for Advanced LIGO.

It should be mentioned here that although the merger rates for NS–NS have been empir-

ically constrained (Kim et al. 2006) no such constrains have been set for BH–BH and BH–NS binaries. The lack of complete understanding of binary stars evolution can lead to merger rate estimations for these systems which vary significantly, depending on the exact physics adopted in the various binary evolution codes. Current effort is focusing on decreasing these uncertainties and setting more solid constraints on the merger rates of BH–NS and BH–BH binaries (O'Shaughnessy et al. 2005, 2006).

Along with the binary evolution studies that provide merger rates of compact binaries, general relativistic calculations of binary mergers try to guide the search for GW signals by predicting the exact shape of the signals and generating GW search templates (e.g., Buonanno et al. 2006; Baker et al. 2006; Abbott et al. 2006; Apostolatos 1995). It is expected that both the BH spin and its misalignment with respect to the orbital angular momentum will affect significantly the shape of the GW signal and its detectability as well (Apostolatos 1995; Grandclement et al. 2003).

Another interesting aspect of BH–NS and NS–NS binaries is their possible connection to the observed short gamma-ray bursts (GRBs), a scenario that has gained widespread support over the last few years, both because of the rapid progress in theoretical modelling and the recent *Swift* observations of short GRBs (see Nakar 2007, for a recent review).

GRBs are classified into two duration classes, separated at $\sim 2\,\mathrm{s}$ (Kouveliotou et al. 1993). Long bursts are found to be predominantly in active star-forming regions. It is now believed that long bursts are produced when a massive star reaches the end of its life, its core collapsing to form a BH and in the process, ejecting an ultra-relativistic outflow (e.g., Woosley & Bloom 2006). The standard collapsar model predicts that a broad-lined and luminous Type I-c core collapse supernova (SN) accompanies long bursts (MacFadyen & Woosley 1999). This association has been confirmed in observations of several nearby GRBs (e.g., Galama et al. 1998; Hjorth et al. 2003; Pian et al. 2006; Gehrels et al. 2006).

Until recently, afterglow of short bursts have been extremely elusive. This situation changed dramatically in 2005. *Swift* and *HETE-2* detected X-ray afterglows from short bursts (Gehrels et al. 2005; Villasenor et al. 2005). This has lead to identification of host galaxies and to redshift measurements. More than ten short burst afterglows were detected so far, and distinctive features emerge. While long bursts occur only in star forming spiral galaxies, short bursts appear also in elliptical galaxies which are dominated by an old star population. The low level of star formation makes it unlikely that the burst originated in a SN explosion. Even though a short burst GRB 050709 took place in a galaxy with current star formation, optical observations ruled out a SN association (Fox et al. 2005). The isotropic energy for short bursts is 2-3 orders of magnitude lower than that for long bursts $E_{iso} \sim 10^{52-54}\,\mathrm{erg}$ (Barthelmy et al. 2005). These results suggest that compact stellar

mergers are the progenitors of short bursts .

The similarity of X-ray afterglow light curves of long and short bursts indicates that afterglows of both classes can be described by the same paradigm, despite of differences in the progenitors. This view is supported by the fact that the decay rate of short burst afterglows is the value expected from the standard fireball model (e.g. Piran 2004; Mészáros 2006), and that at least in two short bursts GRB 050709 and GRB 01221A there is evidence for a jet break (Fox et al. 2005; Soderberg et al. 2006; Burrows et al. 2006). In the standard afterglow model, these breaks are interpreted as a signature of collimation of a fireball into a jet with an opening angle $\theta \sim$ 6-12 degrees and imply beaming-corrected energy of $E \sim (0.5 - 3) \times 10^{49}$ erg, much less than that of long bursts $E \sim 10^{51}$ erg (Frail et al. 2001). The lower energy implies that the mass of the debris torus formed during the merger could be smaller than that of the torus formed in the collapse of the core of massive stars.

Combined with the lack of a jet break in GRB 050724 which gives lower limits of $\theta > 25$ degrees and $E > 4 \times 10^{49}$ erg (Grupe et al. 2006), the current small sample indicates that the outflow of short bursts is less strongly collimated than most previous-reported long GRBs with the median value $\theta \sim 5$ degrees (Frail et al. 2001; however see also Monfardini et al. 2006). The wider jet angle is consistent with a merger progenitor scenario (e.g., Mészáros, Rees & Wijers 1999), since there is no extended massive stellar envelope as in long GRBs that serves to naturally collimate the outflow. More bright short bursts will be needed to improve the jet break statistics substantially.

One of unexpected finds by *Swift* is that early X-ray afterglows of long bursts show a canonical behavior, where light curves include three components: (1) a steep decay component, (2) a shallow decay component and (3) a "normal" decay component. On top of this canonical behavior, many events have superimposed X-ray flares (e.g., Zhang et al. 2006). The X-ray afterglow of a short burst GRB 050724, associated with an elliptical host galaxy, also resembles the canonical light curve, and it suggests a long-lasting engine. A flare at ~ 100 s in the X-ray light curve decays too sharply to be interpreted as the afterglow emission from a forward shock, but is consistent with the high latitude emission from a fireball (Barthelmy et al. 2005; Kumar & Panaitescu 2000). This is appropriate for the late internal shock scenario as invoked to interpret X-ray flares in long GRBs. This interpretation requires that the central engine remains active upto at least ~ 100 s, and challenges simple merger models, because the predicted typical time scale for energy release is much shorter.

Another interesting scenario associated with BH–NS and NS–NS binaries is the possible connection of their mergers to the production of r-process elements (a very important process for the formation of heavy nuclei with $A > 90 - 100$). It is still not clear today what

is the astrophysical site that can provide the appropriate conditions for r-process nucleosynthesis to take place, although the conditions themselves can be estimated (Jaikumar et al. 2006). The possible ejection of extremely neutron-rich ($Y_e \sim 0.1$) material from NS disruptions in compact binary mergers is believed to be a promising source for r-process elements (Lattimer & Schramm 1974,1976). As such mergers are expected to happen in the outskirts of galaxies (Perna & Belczynski 2002), it is possible that the high-velocity ejecta will enrich the intergalactic medium with high mass r-process elements (Rosswog 2005).

Motivated by all these recent observational and theoretical developments, we have embarked on a numerically investigation of the merger process for BH–NS binaries using a 3-D relativistic SPH code. In this paper, the first of a series, we present our methods and numerical code, as well as the results from a first set of preliminary calculations aimed at exploring broadly the parameter space of these mergers. Our paper is organized as follows: In §2 we discuss the SPH code used for our simulations, we develop some analytic considerations regarding the metric used by the code, and we also discuss the various test calculations that we have run. In §3 we present results from our simulations of equatorial mergers (§3.1) and inclined mergers (§3.2), including a discussion of how to set up initial conditions for the inclined case. Finally, a summary and conclusions are given in §4.

2. Methods and Tests

2.1. Critical Radii

Fig. 1[1] shows why the final merger of a BH–NS binary (for a typical stellar-mass BH) is interesting but also particularly difficult to compute: the tidal (Roche) limit is typically right around the ISCO and the BH horizon. On the one hand, this implies that careful, fully relativistic calculations are needed. On the other hand, it also means that the fluid behavior and the GW signals could depend sensitively (and carry rich information) on both the masses and spins of the compact objects, and on the NS EOS. How much information is carried about the fluid depends on where exactly the tidal disruption of the NS occurs: for a sufficiently massive BH, the horizon will always be encountered well outside the tidal limit, in which case the NS behavior remains point-like throughout the merger and disruption will never be observed by a distant observer. If the BH's mass is such that the tidal limit exists outside the horizon, then the GW signal of the disruption could be detected by ground-based

[1]e.g., see Lai et al. (1994) and Wiggins & Lai (2000) for analytical calculations and discussion of tidal radii.

interferometers.

For those cases where disruption occurs outside the BH's horizon, the final outcome of the merger depends strongly on the relative positions of the tidal radius R_t (i.e., the point where disruption takes place) to the ISCO of the BH. Fig. 1 gives a useful description of that and a first idea of what one could expect the outcome to be for mergers of various mass ratios. An interesting fact that we notice first is that for a given BH mass the relative position of R_t to the ISCO changes with the BH's angular momentum: as the BH's spin increases it drags the ISCO further closer to the BH. For high enough mass ratios (low BH mass of the order of a few $M_\odot$) the tidal radius is always encountered outside the ISCO even for non-rotating BHs. For a $10\,M_\odot$ BH, ISCO and R_t coincide for a Schwarzschild BH, but the ISCO moves inside R_t for Kerr (spinning) BHs of that mass. Finally, for higher mass BHs of $\sim 15\,M_\odot$ the situation becomes more interesting as the ISCO lies well outside the tidal radius for a non-spinning BH and for Kerr BHs with low spin, but it starts migrating inside R_t as the BH's angular momentum increases. For highly spinning BHs the tidal radius is encountered well outside the ISCO. Of course for more massive BHs, R_t is not only inside the ISCO but inside the horizon as well, even for the case of an extremal Kerr BH (this happens for $M \gtrsim 100\,M_\odot$).

Why this whole discussion is interesting, is because disruption outside the ISCO could lead to the formation of a disk of the NS debris outside the BH's horizon. If the disruption is to happen inside the ISCO, no such feature is expected to form. Knowing the relative position of ISCO and R_t for various mass ratios for the binary, gives us a first insight on what to expect as an outcome of the merger and in which mass ratios we should look for certain outcomes.

2.2. Analytic Considerations

The SPH code makes use of the Kerr-Schild (K-S) form of the Kerr metric. In this section we summarize the reasons for choosing to use the K-S metric (i.e., its advantages over the Kerr metric in Boyer-Lindquist [B-L] coordinates) and how quantities such as the BH horizons and the angular velocity of equatorial circular orbits around the BH translate from one coordinate system to the other. The reader can find extensive discussions on the B-L and K-S coordinate systems in e.g., Chandrasekhar (1983); Poisson (2004); Kerr (1963). Here, we present a short overview with emphasis on some useful aspects of the K-S metric that relate directly to our calculations and to the representation of our results.

The Kerr solution in B-L coordinates is given by the familiar expressions (Boyer-Lindquist

1967)

$$ds^2 = -(1 - \frac{2Mr}{\Sigma})dt^2 + (\frac{\Sigma}{\Delta})dr^2 + \Sigma d\theta^2$$

$$+ (r^2 + a^2 + \frac{2Mra^2}{\Sigma}\sin^2\theta)\sin^2\theta d\phi^2 - \frac{4Mra\sin^2\theta}{\Sigma}d\phi\, dt \tag{1}$$

where

$$\Delta = r^2 - 2Mr + a^2 \tag{2}$$

$$\Sigma = r^2 + a^2\cos^2\theta. \tag{3}$$

This form has only one off-diagonal term and is therefore far more convenient to use than the K-S form of the metric.[2] Yet, it carries some extra coordinate singularities which correspond to the roots of Δ : $r_\pm = M \pm \sqrt{M^2 - a^2}$ (r_+ and r_- are the future and past horizons respectively, with r_+ only being an event horizon). It is useful to observe that: (a) for $a/M = 1$ the two coordinate singularities (horizons) coincide, (b) for $a/M = 0$ there is only one horizon at $r_h/M = 2$ and the curvature singularity at $r/M = 0$. The obvious advantage of casting the Kerr metric into its K-S form is that one avoids the coordinate singularities at the horizon present in B-L coordinates.

The coordinate singularity at the horizon present in the B-L form of the metric has the following effect (Poisson 2004): although it takes a finite proper time for a particle to cross the event horizon, it takes infinite t time to do so. Also, since the angular velocity $d\phi/dt$ tends to a finite limit at the horizon, ϕ has also to increase an infinite amount : $\phi \to \infty$ (ϕ, like t, is not a "good" coordinate at the horizon). What that practically means for our code is that, it prevents us from extending our calculations all the way to the horizon of the BH. In that case, one needs instead to place an absorbing boundary outside the BH's horizon. Fortunately there is a way to overcome that problem. In order to extend the Kerr metric beyond the horizon, another coordinate system needs to be adopted. Keeping in mind that the horizons are null surfaces, it makes intuitively sense to construct the new coordinates in terms of the null geodesics.

The null geodesics in the Kerr space-time are given by the tangent vectors

$$\frac{dt}{d\tau} = \frac{r^2 + a^2}{\Delta}E \tag{4}$$

[2]Note that this form of the Kerr metric reduces to the well known Schwarzschild solution in the limit $a = 0$: $ds^2 = -(1 - \frac{2M}{r})dt^2 + (1 - \frac{2M}{r})^{-1}dr^2 + r^2 d\theta^2 + r^2\sin^2\theta d\phi^2$

$$\frac{dr}{d\tau} = \pm E \tag{5}$$

$$\frac{d\theta}{d\tau} = 0 \tag{6}$$

$$\frac{d\phi}{d\tau} = \frac{a}{\Delta} E \tag{7}$$

where E is the specific energy.

The real null vector $\vec{l}$ reads:

$$l^{\alpha} = \frac{1}{\Delta}(r^2 + a^2, \pm\Delta, 0, a). \tag{8}$$

Setting $E = 1$ (and using λ for the affine parameter)

$$\frac{dt}{d\lambda} = \frac{r^2 + a^2}{\Delta}, \frac{dr}{d\lambda} = \pm 1, \tag{9}$$

$$\frac{d\theta}{d\lambda} = 0, \frac{d\phi}{d\lambda} = \frac{a}{\Delta}. \tag{10}$$

By choosing the positive sign for $dr/d\lambda$ we obtain an outgoing congruence with the tangent vector field defined by

$$l^{\alpha}\vartheta_{\alpha} = \frac{r^2 + a^2}{\Delta}\vartheta_t + \vartheta_r + \frac{a}{\Delta}\vartheta_{\phi}. \tag{11}$$

The new variables u and $\tilde{\phi}$ can be introduced in the place of t and ϕ:

$$du = dt - \frac{r^2 + a^2}{\Delta} dr \tag{12}$$

$$d\tilde{\phi} = d\phi - \frac{a}{\Delta} dr. \tag{13}$$

The null geodesic now becomes

$$l^{\alpha} = (0, 1, 0, 0) \tag{14}$$

and the metric takes the form

$$ds^2 = -(1 - \frac{2M\tilde{r}}{\Sigma})du^2 + \Sigma d\theta^2 - 2du\, d\tilde{r} - \frac{4aM\tilde{r}\sin^2\theta}{\Sigma} du\, d\tilde{\phi} + 2a\sin^2\theta d\tilde{r}\, d\tilde{\phi}$$

$$+ (\tilde{r}^2 + a^2 + \frac{2M\tilde{r}a^2\sin^2\theta}{\Sigma})\sin^2\theta d\tilde{\phi}^2 \tag{15}$$

where $\tilde{r}$ is defined by[3]

$$\tilde{r}^4 - (\rho^2 - a^2)\tilde{r}^2 - a^2z^2 = 0 \tag{16}$$

with[4]

$$\rho^2 = x^2 + y^2 + z^2. \tag{17}$$

By instead choosing the negative sign for $dr/d\lambda$ we can obtain an ingoing congruence with the tangent vector field given by

$$l'^{\alpha}\vartheta_{\alpha} = \frac{r^2 + a^2}{\Delta}\vartheta_t - \vartheta_r + \frac{a}{\Delta}\vartheta_{\phi} \tag{18}$$

The new variables to be introduced here are

$$dv = dt + \frac{r^2 + a^2}{\Delta}dr \tag{19}$$

$$d\tilde{\phi}' = d\phi + \frac{a}{\Delta}dr \tag{20}$$

In this coordinate system the null geodesic simplifies to

$$l'^{\alpha} = (0, -1, 0, 0) \tag{21}$$

and the metric becomes

$$ds^2 = -(1 - \frac{2M\tilde{r}}{\Sigma})dv^2 + \Sigma d\theta^2 + 2dvd\tilde{r} - \frac{4aM\tilde{r}\sin^2\theta}{\Sigma}dvd\tilde{\phi}' - 2a\sin^2\theta d\tilde{r}d\tilde{\phi}'$$
$$+ (\tilde{r}^2 + a^2 + \frac{2M\tilde{r}a^2\sin^2\theta}{\Sigma})\sin^2\theta d\tilde{\phi}'^2 \tag{22}$$

What's the use of those two different coordinate sets? The coordinates (v,r,θ,$\tilde{\phi}'$) are well behaved on the future horizon, yet they are singular on the past horizon, where (u,r,θ,$\tilde{\phi}$)

---

[3]a more geometrically insightful representation of Eq. (16) would be:

$$\frac{x^2 + y^2}{\tilde{r}^2 + a^2} + \frac{z^2}{\tilde{r}^2} = 1$$

[4]Note that as $a \to 0$, $\tilde{r} \to \rho$

are now well behaved. Therefore the first set of coordinates is used in order to regularize the past horizon, whereas the second one is used to regularize the future horizon. If one wants to avoid both horizons of a Kerr BH, both patches need to be used in order to cover the entire spacetime around the BH. Then there is just the curvature singularity of the Kerr metric left, which occurs at

$$\Sigma = \tilde{r}^2 + a^2 \cos^2\theta = 0 \Rightarrow \tag{23}$$

$$x^2 + y^2 = a^2 \tag{24}$$

The curvature singularity is not a point but rather a ring of radius a and exists only at the equatorial plane. It is always found inside the past horizon, although as a/M decreases the curvature singularity and the past horizon approach each other (Fig. 2).

2.3. SPH Code

We employ a 3-D implementation of the SPH technique. The GRSPH (General Relativistic Smooth Particle Hydrodynamics) code is based on the work by Laguna et al. (1993a) in which the general relativistic hydrodynamic equations were rewritten in a Lagrangian form similar to their counterparts for non-relativistic fluids with Newtonian self-gravity. The GRSPH code is restricted to fixed curved spacetimes, in particular the spacetime of a rotating black hole. Originally the black hole metric used in the code was in terms of Boyer-Lindquist coordinates. For the present work, we use Kerr-Schild coordinates. The main advantage of these coordinates is their regularity across the black hole horizon, thus allowing SPH particles to freely cross it. An important aspect of SPH in curved spacetimes is the handling of the local volume averages required by the smoothing of the equations. The smoothing volumes involved are in general not small enough to ignore curvature effects, in particular in the neighborhood of the black hole. Our implementation correctly accounts for these effects. The most important computational aspect of the GRSPH code is the particle neighbor finding algorithm. The GRSPH code uses an *oct-tree* data structure as basis for finding neighbors (Warren & Salmon 1991). The oct-tree in GRSPH has been successfully used for N-body large-scale structure simulations (Heitmann et al. 2005) and used as a foundation of a SPH code with radiation transport (Fryer et al. 2006). The GRSPH code scales as $O(N \log N)$ with N the number of particles . The code was calibrated with three one-dimensional benchmarks (Laguna et al. 1993): (1) relativistic shock tubes, (2) dust infall onto a black hole, and (3) Bondi collapse (see Laguna et al. 1993a for the details). The code has been successfully applied to studies of the tidal disruption of main sequence stars by a supermassive BH (Laguna et al. 1993b; Kobayashi et al. 2004; Bogdanovic et al. 2004).

The use of a fixed background in our simulations is justified for low mass ratios ($q \simeq 0.1$

in this paper) where the mass of the BH is substantially larger than the NS mass. Artificial viscosity is implemented in our code by following the description presented in Laguna et al. (1993a) and Laguna et al. (1994). Artificial viscosity is a mechanism for accounting for the possible presence of shocks and is introduced as a viscous pressure term added to the SPH equations (Laguna et al. 1993a). As we do not expect any shocks to appear anywhere but perhaps at the point where the stream of NS material accreting onto the BH crosses itself, we keep artificial viscosity suppressed by lowering the parameters of its two terms (the bulk viscosity term and the von Neumann-Richtmyer (1950) viscosity term) at the value 0.2 instead of order unity that is commonly used (see Laguna et al. 1993a, for details and tests).

Radiation reaction is implemented in the GRSPH code by following the prescription described in Lee & Kluzniak (1999b), §2. We use the quadrupole formula for the rate of energy radiated (Eq. (4) in Lee & Kluzniak 1999b) to derive a damping force (Eq. (6) in Lee & Kluzniak 1999b) for each of the SPH particles. The formula has been slightly modified as in our code we deal with du/dt where u is the 4-velocity. We have also added a parameter to increase the radiation reaction force in order to accelerate the inspiral since we do not want to spend too much computational time for it. We have checked that once the inspiral starts, this parameter does not make much difference. It has the effect of putting the NS in a plunge trajectory.

Throughout our calculations and for all the results presented here we use geometrized units with $G = c = 1$.

2.4. Test Calculations

2.4.1. Testing the K-S Metric

The Kerr-Schild coordinate system used in the SPH code is only avoiding the outer (future) horizon, since that serves the purpose of the SPH particles getting as close to the BH's horizon as possible, without the code crashing or becoming problematic. Yet, in the extremal Kerr case ($a/M = 1$), the two horizons coincide (Fig. 2) at $\tilde{r} = \sqrt{2}M$, and as a result, we see the orbits of the SPH particles being trapped at $\tilde{r} = \sqrt{2}M$. To check that it is the inner horizon where our transformation is singular, we set up the following simple test: we construct a test particle geodesic integrator that makes use of the K-S metric and we start with an equatorial orbit for $a/M = 1$ which, starting from a finite distance from the BH (having $v_z = v_y = y = z = 0$), ends being trapped at $\tilde{r} = \sqrt{2}M$. We then keep following the same orbit as we reduce the value of a (Fig. 3). The result is that the particle ends being trapped at the inner horizon (whichever that is for the specific value of a). The trapping

is illusionary: it reveals the singularity of our coordinate transformation. We thus avoid using $a/M = 1$ in the simulations presented in this paper and instead we set $a/M = 0.99$ for the case of an extremal Kerr B.H. By doing so, the future horizon moves outwards at $\tilde{r}_+ = 1.51067M$ and the past horizon moves inwards at $\tilde{r}_- = 1.31067M$ and are therefore distinguishable.

Another quantity that is going to be affected by the coordinate transformation (i.e., from B-L to K-S) is the angular velocity Ω_ϕ for a circular equatorial orbit around the BH. In B-L coordinates Ω_ϕ is given by

$$\Omega_\phi = \pm \frac{M^{1/2}}{r^{3/2} \pm aM^{1/2}} \tag{25}$$

where $r^2 = x^2 + y^2 + z^2$ and the upper (lower) sign corresponds to co-rotating (counter-rotating) orbits. In K-S coordinates Eq. (25) holds when r is replaced by $\tilde{r}$, as defined by Eq. (16) (see Appendix C for an analytical calculation of Ω_ϕ in K-S coordinates). In order to check numerically that this is the correct formula for Ω_ϕ, we set up the following test: we use again the geodesic integrator and we place a test particle at some distance r_0 from the BH and give it the angular velocity that corresponds to an equatorial circular orbit at the specific r_0 as required by Eqs. (25) and (16). As expected, the test particle remains in this fixed circular orbit (with $d\tilde{r}/d\tau = 0$) as we integrate for a large number of orbital periods. If we instead use Eq. (25) with $r^2 = x^2 + y^2 + z^2$, the particle follows an oscillating orbit ($dr/d\tau \neq 0$) around its initial position, indicating that the formula used for Ω_ϕ needs modification.

2.4.2. Stable Binary Orbits

In a first test, we considered a white dwarf (WD) with $M_* = 0.6\,M_\odot$ and $R_* = 1.3 \times 10^{-2}\,R_\odot \sim 9 \times 10^8\,\mathrm{cm}$ orbiting around a Schwarzschild BH with $M = 2 \times 10^5\,M_\odot$. Here 5000 particles are used to represent the WD with a $\Gamma = 5/3$ polyt,ropic EOS. Since the mass ratio is extreme, our approximation (moving the fluid on a fixed background metric) should be extremely accurate. With these parameters, the tidal radius $R_t \sim 6.3 \times 10^{10}$cm and the horizon scale $r_h = 2M \sim 5.9 \times 10^{10}\,\mathrm{cm}$ are comparable, and much larger than the WD radius R_*. If $R_t \gg r_h$, the point particle approximation should break down for orbits near the ISCO because the WD will get disrupted at radii well outside the ISCO. On the other hand, when $R_t \ll r_h$, the sound crossing time of the WD is much shorter than the orbital period, and it is numerically expensive. Thus, we have chosen the parameters satisfying $R_t \sim r_h$ to test the code for relativistic orbits. With these parameters we found that we can maintain

a circular orbit at $r = 8\,M$ to within $|\Delta r|/r < 10^{-3}$ over one full orbital period (Fig. 4).

In a second, similar test we considered a NS with $m = 1.4\,M_\odot$ and $R_{NS} = 13.4\,\mathrm{km}$ $= 1.93 \times 10^{-5}\,R_\odot$ (represented by 10000 SPH particles and with a $\Gamma = 2$ polytropic EOS) orbiting around a Schwarzschild BH with $M = 10\,M_\odot$. We found that we can maintain a NS orbiting at $r = 20\,M$ stably and without any noticeable numerical dissipation for more than 20 orbital periods.

2.5. Initial Conditions for BH–NS Binaries

We set up initial conditions for BH–NS binaries near the Roche limit using the SPH code and a relaxation technique similar to those used for previous SPH studies of close binaries (e.g., Rasio & Shapiro 1995). First we construct hydrostatic equilibrium NS models for a simple gamma-law EOS by solving the Lane-Emden equation. When the NS with this hydrostatic profile is placed in orbit near a BH, spurious motions could result as the fluid responds dynamically to the sudden appearance of a strong tidal force. Instead, the initial conditions for our dynamical calculations are obtained by relaxing the NS in the presence of a BH in the co-rotating frame of the binary. For *synchronized* configurations (assumed here), the relaxation is done by adding an artificial friction term to the Euler equation of motion in the co-rotating frame. This forces the system to relax to a minimum-energy state. We numerically determine the angular velocity Ω corresponding to a circular orbit at a given r as part of the relaxation process. The advantage of using SPH itself for setting up equilibrium solution is that the dynamical stability of these solutions can then be tested immediately by using them as initial conditions for dynamical calculations.

3. First Results

3.1. Equatorial BH–NS Mergers for Spinning and Non-spinning BH

For all the results presented in this section we ran simulations using 10^4 SPH particles to represent a NS with a $\Gamma = 2$ polytropic EOS. The NS mass is $m = 1.4 M_\odot$ and its radius is $R_{NS} = 15\,\mathrm{km}$. The BH has a mass $M = 15 M_\odot$. All the SPH particles are of equal mass ($m_p = m/10^4$). The NS is initially placed at a distance $r_0 = 8M$ and for the cases of a spinning BH ($a/M \neq 0$) the NS is co-rotating in the equatorial plane. The angular momentum of the BH is left as a free parameter.

As a first approach we would like to get an idea on the possible outcome of a BH–

NS merger: what percentage -if any- of the NS mass survives the merger, which are the morphological features of the merger (e.g., creation of accretion disk, spread of the accreting material), and how the BH angular momentum affects these features. For the two extreme cases $a/M = 0$ and $a/M = 0.99$ (we avoid using $a/M = 1$ for the reasons mentioned in §2.2), we observe a completely different behavior.

Fig. 5 shows the outcome of the merger for a non spinning BH: the NS, after being completely disrupted and following an inspiraling orbit, disappears entirely into the BH's horizon in a time $t/M \simeq 180$ after the beginning of the simulation (where t is the coordinate time for an observer at inifinity).

The result of our simulation for the case of the extremal Kerr BH ($a/M = 0.99$) is shown in Figs. 6 and 7. The NS again gets completely disrupted and falls toward the co-rotating BH following an inspiraling orbit while an outwards expanding tail of the disrupted NS's material is forming at the same time. The NS fluid starts disappearing into the BH's horizon at $t/M \simeq 400$ with an initially high infall rate which finally diminishes to an almost zero level. At this point ($t/M = 490$) about 30% of the initial NS mass resides outside the BH's horizon (Fig. 8). We notice that the disruption takes place well outside the ISCO, in contrast to the previous case of a Schwarzschild BH.

We run the same exact type of simulations for different values of the BH's angular momentum and compare the results. Fig. 8 shows the fraction of the initial NS mass that survives the merger for five different values of a/M ($0.75 \leq a/M \leq 0.99$). As the angular momentum of the BH decreases, so does the fraction of material that survives, residing outside the BH's horizon. For the case of $a/M = 0.1$ (not included in the latter figure for practical reasons), the situation is almost the exact same as for the Schwarzschild (non-spinning) BH: the NS disappears completely into the horizon (Table 1 summarizes our results).

For the simulations with a/M spanning the range $0.1 < a/M < 0.75$, namely for $a/M = 0.2$, $a/M = 0.5$ and $a/M = 0.6$, we observe that the infall starts earlier as a/M decreases (consistent with the behavior of the high a/M mergers). No surviving material exists for those mergers with low spin for the BH ($a/M < 0.7$).

The morphological features of the mergers for the non-maximally spinning BH are similar to the extremal case, with the difference that, as a/M decreases the outwards expanding tail tends to spread less. For the very low a/M cases no such tail is forming.

By the end of the SPH simulations, the mass fraction that resides outside the BH's future horizon seems to have reached a stable value. Since for $a/M \geq 0.9$ there is substantial part of the NS's mass surviving the merger, one would like to investigate what the final fate of this material might be, i.e., what percentage of it -if any - will escape or stay bound

forming a stable disk around the BH. To answer those questions we first calculate the rest energy (energy as measured by an observer at infinity) of each SPH particle throughout the whole simulation for runs E1-E5. By knowing a particle's energy we can determine whether it is bound or unbound ($e^2 > 1$ for unbound and $e^2 < 1$ for bound[5], where $e = -(g_{tt}u^t + g_{t\phi}u^\phi + g_{tr}u^r)$ is the rest energy per unit mass for an observer at infinity). Fig. 9 show the variations of bound and unbound mass for each of our simulations.

For the two runs with the highest a/M values (runs E1 and E2 from Table 1) we are able to resolve a non zero fraction of bound material ($2-3\%$ of the NS's mass). For runs E3, E4 and E5 the percentage of bound material drops to unresolvable values (as mentioned at the beggining of this paragraph the code's mass resolution is $m_p = m/10^4$). As shown in Fig. 9 for the runs E1 and E2, both the unbound and bound NS material stabilize at a certain value and persist there for a long time. That leads us to believe that the bound fraction of the surviving mass stays around the BH forming a stable disk. In order to check whether our definition of bound and unbound material is correct, we do the following test-runs: we evolve the results of the SPH simulations using again the geodesic integrator. For every different run (different a/M) we set as initial conditions for the geodesic integrator the last output file from the equivalent SPH simulation. We make sure to run the geodesic integrator for a sufficiently long time as it is much faster than the SPH code. The results of those tests, met our expectations.

Namely, the material that we recognized as unbound escapes completely following parabolic trajectories, whereas the particles that were energetically determined to be bound (for runs E1 and E2 only) remain bound around the BH (and outside the BH's horizon) following equatorial precessing orbits, with maximum apoastron $\sim 30M$, minimum periastron of about $\sim 2-3M$ and a very small dispersion towards the direction of the BH's axis $\sim 0.1-0.2M$ (see Fig. 10).

Two important remarks on the results of Table 1: no substantial fraction of bound material survives for mergers with $a/M \lesssim 0.95$ and therefore no formation of a stable disk is observed, and also for the cases with $a/M \lesssim 0.7$ the merger is completely catastrophic for the NS, with no material surviving the merger.

---

[5]for an analytical discussion and a proof of that see Wilkins (1971) and Chandrasekhar (1983, chap.3, §19)

3.2. Non-equatorial BH–NS Mergers

Many authors have suggested that a significant NS birth kick is required for the formation of coalescing BH–NS binaries (e.g., Kalogera 2000; Lipunov et al. 1997). Any misalignments between the axis of the BH and the NS progenitor are expected to be canceled during the evolution of the binary prior to the supernova (SN) explosion that is associated with the formation of the NS, due to mass-tranfer phases. Any spin-orbit misalignement therefore is expected to be introduced by the SN that forms the NS. Kalogera (2000) argues that tilt angles greater than 30^o are expected for $30\% - 80\%$ of coalescing BH–NS binaries, whereas tilt angles of $50^o - 100^o$ are expected for at most 70% of such systems. In order to account for these findings, we set up some simulations for misaligned mergers, covering a wide range of tilt angles from $30^o - 180^o$. The results are presented in the two following subsections.

3.2.1. Setting Up Initial Conditions

The selection of initial conditions for the equatorial mergers is straight forward: select an initial radius r_0 -outside the Roche limit- and calculate the angular velocity Ω_ϕ needed for the relaxation procedure using Eqs. (25) and (16). Obviously, Eq. (25) does not hold for non-equatorial orbits, since its derivation assumes that $\theta = \pi/2$. When moving away from the equatorial plane, there is a third constant of the motion[6] appearing (the Carter constant Q), as a result of the existence of a killing tensor. (The geodesics equations of the Kerr spacetime are included in Appendix B). In order to find a stable, so-called spherical, non-equatorial orbit on which to initially place the NS, we follow the technique described in Hughes (2000). (For an in depth analysis of the procedure, refer to Hughes 2000 and Wilkins 1971). Here, we point out the basic steps for finding and setting up numerically the initial conditions for such an orbit, as presented in Hughes (2000).

For a circular orbit $R(\equiv dr/d\tau) = 0 = R'$, where the prime indicates differentiation with respect to τ . Furthermore, for the orbit to be stable $R'' < 0$ should also hold. One can specify a unique orbit by fixing r_0 and L_z. The conditions $R = 0 = R'$ will fix the other two parameters of the orbit, E and Q. The inclination of the orbit (which is a constant of the motion) can be calculated as :

$$\cos(i) = \frac{L_z}{\sqrt{L_z^2 + Q}} \tag{26}$$

[6]the other two being the energy E and angular momentum L_z, related to the stationary and axial Killing vectors respectively.

(with i being zero on the equatorial plane where the Carter constant Q is also zero).

The most bound orbit (in terms of energy) for a given radius r_0 is the equatorial prograde orbit (in the same sense the retrograde orbit corresponds to the least-bound orbit). Therefore, one can start by choosing a radius r_0 in the equatorial plane (where $Q = 0$) and then, by solving $R = 0 = R'$, calculate the energy E and angular momentum L_z for that orbit. Solving analytically the condition (with R being defined by Eq. (B1)) one gets for the prograde and retrograde orbits (Hughes 2000)

$$E^{pro} = \frac{1 - 2v^2 + pv^3}{\sqrt{1 - 3v^3 + 2pv^3}} \tag{27}$$

$$L_z^{pro} = rv\frac{1 - 2pv^3 + p^2v^4}{\sqrt{1 - 3v^2 + 2pv^3}} \tag{28}$$

$$E^{ret} = \frac{1 - 2v^2 - pv^3}{\sqrt{1 - 3v^3 - 2pv^3}} \tag{29}$$

$$L_z^{ret} = -rv\frac{1 + 2pv^3 + p^2v^4}{\sqrt{1 - 3v^2 - 2pv^3}} \tag{30}$$

where $v = \sqrt{M/r}$ and $p = a/M$.

With E and L_z numerically known for a given equatorial orbit of radius r_0, one can proceed into finding non-equatorial stable orbits. The way to do so is by keeping the radius r_0 fixed, decreasing the value of L_z and solving again for the conditions $R = 0 = R'$, which now are going to give the energy and Carter constant. This way one can keep on decreasing the value of L_z until it reaches the value L_z^{ret} or until $R'' = 0$ (marginally bound). The stability of the new, inclined orbit (with the inclination given by Eq. (26)) should be checked with the requirement $R'' < 0$. The angular velocity of this orbit can now be numerically determined as $\Omega_\phi = d\phi/dt$ by using the geodesics equations for $d\phi/d\tau$ and $dt/d\tau$ (Eqs. (B3) and (B4)). The velocity for a stable, spherical, non-equatorial orbit of radius r_0 and inclination i will be $v_y = r_0\Omega_\phi \cos(i)$

Since we have followed this numerical method to find initial conditions for the inclined mergers, tuning the r_0 and L_z values in order to solve for an exact value of inclination angle was not trivial to do. In any case we tried to get as close to the value of the desired inclination angle as it was numerically possible. For example, the inclined merger labelled to be 30^o was in reality 29.6577^o. Similar order deviations of the integer value of inclination hold for the rest of the inclined mergers presented here.

3.2.2. Results

We have run five simulations of non-equatorial mergers, for five different inclination angles all with $a/M = 0.99$ (Table 2). The rest of the characteristics of the simulations presented in this section, i.e., BH and NS masses, polytropic index Γ, number of SPH particles, are as mentioned in §4.1 .

Runs I4 ($i \approx 90^o$) and I5 (retrograde orbit) end up with the NS being entirely lost into the BH's horizon after spiraling around it for several orbits. The difference between the outcomes of those two mergers is that, for run I4 the 'feeding' of the BH does not take place on the equatorial plane: the NS follows a 3D spherical orbit of decreasing radius before it finally vanishes completely into the BH.

The outcome of Run I1 is presented in Figs. 11 and 12. As in the equatorial mergers of high a/M presented in §4.1, the merger results in the formation of an expanding tail of the NS's material, with the innermost part of the helix 'feeding' the BH. For this case the helix does not lay on the equatorial plane , although the feeding point does. By the end of the simulation almost 40% of the NS mass remains outside the BH's horizon with most of it unbound and only about 6% bound. We followed the procedure described already in §3.1 and used the geodesic integrator to further evolve the results of the SPH simulation as a test of the validity of our definition of bound and unbound mass and to check the spatial distribution of the bound material around the BH. The whole unbound part of the surviving material escapes outwards, whereas the bound mass forms a stable torus outside the BH's horizon. Fig. 13 shows the spatial distribution of pericenters (in red - upper right and lower panels) and apocenters (in blue - upper left and middle panels) on the x-y and x-z planes. Every particle is depicted at the moment of its own apocenter (or pericenter) (i.e., those plots do not correspond to a snapshot of specific time of the equivalent merger).

Run I2 corresponds to a merger with initial inclination of $\sim 45^o$. As the infall of the NS's material into the BH starts, at about $t/M = 1500$ after the beginning of the simulation, an outwards expanding tail is forming (Figs. 14 and 15) and by the end of the simulation 25% of the initial NS mass (Fig. 16) is left unbound and escaping. No bound, disk-forming material was resolved in this case.

For an inclination of $\sim 70^o$ (Run I3) the outcome of the merger is no different than that of Runs I4 and I5: the whole NS disappears into the BH's horizon. The morphological features of this merger though is somewhere in between those of the low inclination mergers, where there is mass surviving and the higher inclination ones, which ended up being completely catastrophic for the NH. After the NS orbits around the BH following a spherical orbit of decreasing radius, it starts accreting into the BH with the feeding point being well above the

equatorial plane. As the infall continues, the part of the NS that is still outside the BH's horizon moves towards the equatorial plane and at the last stages of the merger, when the feeding point has sufficiently approached the equatorial plane, a small, expanding, spiraling tail forms which is energetically unable to escape or expand significantly and ends up being accreted into the BH as well. At the end of the simulation there is no surviving mass (Fig. 17).

The difference between equatorial and inclined mergers in terms of the surviving bound mass seems to be the vertical (z-axis) distribution of the NS debris. In the first case the bound material remains on an equatorial disk ($-0.15M \leq z \leq 0.15M$) whereas in the later case the disk take the form of a torus with $-1M \leq z \leq 1M$, and also in the later case the torus is more massive than the disk of the equatorial mergers.

We note that the geodesic integrator runs are taken just as an approximation and a qualitative test of the further evolution of the two groups of surviving material (bound and unbound), for the cases where hydrodynamics is of no importance and the SPH particles can be treated as free particles; e.g., for unbound particles at great distances from the BH.

4. Discussion and Summary

We have performed simulations of BH–NS mergers with mass ratio $q \simeq 0.1$ and polytropic index $\Gamma = 2$ using a 3-D relativistic SPH code. We investigated equatorial mergers for various values of the BH spin and we also carried out simulations for inclined mergers (considering a tilted orbital plane for the NS with respect to the BH's equatorial plane) in the case of an extremal Kerr BH. We find that the outcome of the merger depends strongly on the spin of the BH and the inclination of the orbit. More specifically, for equatorial mergers, the survival of NS material is possible only for mergers with $a/M > 0.7$ and, in that case, the percentage of surviving material increases with increasing BH spin, varying from about 35% to $\sim 1\%$ for a/M decreasing from 0.99 to 0.7. Complete disruption of the NS happens for all values of a/M. Most of the surviving material gets ejected from the vicinity of the BH and only a few percent stays bound to the BH, forming a relatively thin stable disk outside the BH's horizon. Only for very high BH spins ($a/M > 0.95$) do we see a substantial fraction ($\sim 3\%$) of the disrupted NS material remaining bound.

The outcome of inclined mergers (for fixed $a/M = 0.99$) shows strong dependence on the value of the inclination angle. For sufficiently low inclinations ($< 60^o$) there is always a large fraction of the NS mass surviving the merger, $\sim 20-40\%$, depending on the inclination angle. Moreover, for these mergers the formation of a thick stable torus of substantial bound

mass is also strongly inclination-dependent. Whenever the inclination exceeds $40 - 45^o$ the fraction of bound material drops to levels unresolvable by our present calculations, although there is still a significant fraction ($\sim 25\%$) of the material that is being ejected.

The complete tidal disruption of the NS in all the merger calculations that we presented in this paper is in qualitative agreement with previous Newtonian studies of BH–NS mergers with *soft* EOS (Rosswog et al. 2004; Lee & Kluzniak 1999b). However, those studies suggested that for a stiffer EOS a core of the NS always survives the merger (Lee & Kluzniak 1999a; Kluzniak & Lee 1998). The general picture that comes out of these Newtonian calculations is that for higher mass ratios (with $q \sim 0.7 - 0.28$) the survival of NS material and formation of a disk around a Schwarzschild BH is possible for soft EOS. For these high mass ratio mergers the tidal disruption radius lies outside the ISCO, which allows for more NS material to settle into a disk after the tidal disruption. A stiffer EOS could, in that case prevent the total disruption of the NS, leading to the formation of a "mini-NS" along with the disk or even lead to multiple disruptions of the surviving NS core. Rosswog et al. (2004) suggested that the surviving of a mini-NS for the case of a stiff EOS ($\Gamma = 3$) and various mass ratios, is connected with the formation of the observed disk in their calculations, arguing that the survival of an orbiting NS core acts as a storage mechanism that prevents further inflow of material towards the BH.

In our simulations that involved a Schwarzschild (non-spinning) BH, no NS material was observed being ejected or forming a disk around the BH. The accretion of the whole NS onto the BH is very prompt for this case. This is to be expected, as for the particular mass ratio ($q \simeq 0.1$) considered in our simulations the tidal limit is found inside the ISCO for $a/M = 0$ and thus we would not expect to find a stable disk forming around the BH. In their full-GR treatment of BH–NS mergers for a non-spinning BH of arbitrary mass, Shibata & Uryu (2006a,b) concluded that the disruption of a NS by a low-mass BH ($M = 3.2 - 4\,M_\odot$) can lead to the formation of a low-mass disk (of mass $\sim 0.1\,M_\odot$) around the BH, which could potentially power a short GRB. No formation of more massive disks was ever observed in their simulations, indicating that systems with $\sim M_\odot$ disks around a BH can not be formed through BH–NS mergers with non-spinning BHs.

Faber et al. (2006b) followed a fully relativistic treatment for their simulations of BH–NS mergers with mass ratio $q = 0.1$ and a non-spinning BH. As mentioned already in this paper, for this specific mass ratio and BH spin, the tidal radius of a NS that has the "expected" mass and radius (i.e., its compactness being $\mathcal{C} = M_{NS}/R_{NS} \sim 0.14 - 0.21$) is found inside the ISCO. For this reason, Faber et al. (2006b) consider undercompact models for the NS ($\mathcal{C} = 0.042$), in order to study cases where the disruption of the NS takes place outside the ISCO. In their paper, they suggest that their study of undecompact NSs can serve as an

analogue for binaries with lower mass BHs and more compact NSs, where the tidal radius is placed well outside the ISCO. They found that (a) there is a small fraction ($\sim 5-7\%$) of the NS mass that becomes unbound and escapes from the system, (b) although most of the infalling mass is accreted promptly, there is a part of it ($\sim 25\%$) that remains bound outside the horizon, forming a disk. We observed no such ejected or disk-forming material for the merger of a NS with compactness $\mathcal{C} = 0.14$ and a Schwarzschild BH, and such an outcome was seen only for mergers with spinning BHs.

In Paper II we will extend our simulations to include different mass ratios, although remaining in the limit where the use of a fixed background is justified (i.e., for BH masses much larger than the NS mass), and we will explore the effects of changing the NS EOS and relaxing our assumption of an initially synchronized NS spin. Ultimately, the adoption of a full numerical relativistic scheme, where no assumptions for a static background are made, would be of great interest, as it would allow us to explore mergers of higher mass ratios. Although the Newtonian studies of those mergers have given a qualitative idea of the possible outcomes, there is a consensus that relativistic effects will play a very significant role in the spatial distribution of the disrupted NS material, which plays a key role for the connection of such mergers to short GRBs

Acknowledgments This work was supported by NSF Grants PHY-024528 and PHY-0601995 at Northwestern University. We thank Scott Hughes and Josh Faber for useful discussions. PL acknowledges the support of the Center for Gravitational Wave Physics at Penn State, funded by the NSF under Cooperative Agreement PHY-0114375, and NSF grants PHY-0244788 and PHY-0555436

A. K-S form of the Kerr metric

Kerr presented his solution for the first time (Kerr 1963) in the following format:

$$ds^2 = (\tilde{r}^2 + a^2\cos^2\theta)(d\theta^2 + \sin^2\theta d\phi^2) + 2(du + a\sin^2\theta d\phi) \times (d\tilde{r} + a\sin^2\theta d\phi)$$
$$- (1 - \frac{2M\tilde{r}}{\tilde{r}^2 + a^2\cos^2\theta}) \times (du + a\sin^2\theta d\phi)^2 \quad \text{(A1)}$$

.

By using:

$$u = t + \tilde{r}$$
$$\tilde{r}\cos\theta = z \quad \text{(A2)}$$
$$(\tilde{r} - ia)e^{i\phi}\sin\theta = x + iy$$

Eq. (A1) can be transformed to an asymptotically flat coordinate system (Kerr 1963). First let's apply $u = t + \tilde{r}$ on Eq. (A1). This will lead to the more familiar form:

$$ds^2 = -(1 - \frac{2M\tilde{r}}{\Sigma})dt^2 + (1 + \frac{2M\tilde{r}}{\Sigma})d\tilde{r}^2 + \Sigma d\theta^2$$
$$(\tilde{r}^2 + a^2 + \frac{2M\tilde{r}}{\Sigma}a^2\sin^2\theta)\sin^2\theta d\phi^2 + \frac{4M\tilde{r}}{\Sigma}dt\, d\tilde{r} \quad \text{(A3)}$$
$$+\frac{4M\tilde{r}}{\Sigma}a\sin^2\theta d\phi\, dt + (1 - \frac{2M\tilde{r}}{\Sigma})2a\sin^2\theta d\phi\, d\tilde{r}$$

where

$$\Sigma = \tilde{r}^2 + a^2\cos^2\theta$$

and $\tilde{r}$ is defined by :

$$\tilde{r}^4 - (\rho^2 - a^2)\tilde{r}^2 - a^2z^2 = 0 \quad \text{(A4)}$$

with $\rho^2 = x^2 + y^2 = z^2$.

Now applying the rest of the transformations in (A2), one gets:

$$ds^2 = dx^2 + dy^2 + dz^2 - dt^2 + \frac{2M\tilde{r}^3}{\tilde{r}^4 + a^2z^2}(k)^2 \quad \text{(A5)}$$

where

$$k = [\frac{\tilde{r}(xdx + ydy) + a(xdy - udx)}{\tilde{r}^2 + a^2} + \frac{z}{\tilde{r}}dz + dt] \quad \text{(A6)}$$

Let us make a useful parenthesis here: to understand better why the transformation rules (A2) were chosen, it is constructive to start with Eq. (A1) and bring it to the following form:

$$ds^2 = [-du^2 + 2du\,d\tilde{r} + \Sigma d\theta^2 + 2a\sin^2\theta d\tilde{r}\,d\phi + (\tilde{r}^a + a^2)\sin^2\theta d\phi^2] + \frac{2M\tilde{r}}{\Sigma}(du + a\sin^2\theta d\phi^2) \tag{A7}$$

.

Eq. (A7) can be interpreted as following: the terms not containing the mass m, give the flat space metric in some coordinate system, while the last term can be expressed in terms of the null (tangent with respect to $\eta_{\alpha\beta}$) vector, l_α:

$$-l_\alpha dx^\alpha = du + a\sin^2\theta d\phi$$

and therefore the line element ds^2 can be written in the form:

$$ds^2 = (ds^2)_{flat} + \frac{2M\tilde{r}}{\Sigma}(l_\alpha dx^\alpha)^2 \tag{A8}$$

and the metric is :

$$g_{\alpha\beta} = \eta_{\alpha\beta} + \frac{2M\tilde{r}}{\Sigma} l_\alpha l_\beta$$

This is actually the original way which Kerr followed to discover his solution.[7]

The idea now is to find those transformations that will take the part of Eq. (A7) that is contained in the brackets to the standard representation of the Minkowski space. This will lead us to the already mentioned transformation rules (A2).

Notice that the metric (A5) is analytical everywhere except at $x^2 + y^2 = a^2$ (or else at $\rho = a$ and $z = 0$).

B. Geodesics of the Kerr spacetime in B-L coordinates

The Kerr geodesics equations (Misner, Thorne & Wheeler 1973)

$$\Sigma^2 \left(\frac{dr}{d\tau}\right)^2 = [E(r^2 + a^2) - aL_z]^2 - \Delta[r^2 + (L_z - aE)^2 + Q] \equiv R \tag{B1}$$

[7]Any metric of the form $g_{\alpha\beta} = \eta_{\alpha\beta} + Hl_\alpha l_\beta$, with H a scalar and l_α a null vector field, is called a Kerr-Schild metric

$$\Sigma^2 \left(\frac{d\theta}{d\tau}\right)^2 = Q - \cot^2\theta L_z^2 - a^2\cos^2\theta(e-e^2) \equiv \Theta \tag{B2}$$

$$\Sigma\left(\frac{d\phi}{d\tau}\right) = \csc^2\theta L_z + aE\left(\frac{r^2+a^2}{\Delta} - 1\right) - \frac{a^2 L_z}{\Delta} \tag{B3}$$

$$\Sigma\left(\frac{dt}{d\tau}\right) = E\left[\frac{(r^2+a^2)^2}{\Delta} - a^2\sin^2\theta\right] + aL_z\left(1 - \frac{r^2+a^2}{\Delta}\right) \tag{B4}$$

C. Ω_ϕ for equatorial orbits in K-S coordinates

The metric in K-S coordinates

$$ds^2 = -(1 - \frac{2M\tilde{r}}{\Sigma})dv^2 + \Sigma d\theta^2 + 2dv\,d\tilde{r} - \frac{4aM\tilde{r}\sin^2\theta}{\Sigma}dv\,d\tilde{\phi}' - 2a\sin^2\theta d\tilde{r}\,d\tilde{\phi}'$$
$$+ (\tilde{r}^2 + a^2 + \frac{2M\tilde{r}a^2\sin^2\theta}{\Sigma})\sin^2\theta\,d\tilde{\phi}'^2 \tag{C1}$$

where

$$\tilde{r}^4 - (x^2+y^2+z^2-a^2)\tilde{r}^2 - a^2z^2 = 0 \tag{C2}$$

$$\Sigma = \tilde{r}^2 + a^2\cos^2\theta. \tag{C3}$$

Restricting the metric on the $\theta = \pi/2$ plane

$$ds^2 = -(1 - \frac{2M}{\tilde{r}})dv^2 + 2dv\,d\tilde{r} - \frac{4aM}{\tilde{r}}dv\,d\tilde{\phi}' - 2ad\tilde{r}\,d\tilde{\phi}' + (\tilde{r}^2 + a^2 + \frac{2Ma^2}{\tilde{r}})d\tilde{\phi}'^2. \tag{C4}$$

Two Killing vectors are associated with the $v-$ and $\tilde{\phi}'-$ invariance or Eq. (C4)

$$\vec{\xi} = (1,0,0,0) \tag{C5}$$

$$\vec{\eta} = (0,0,0,1) \tag{C6}$$

and the defined conserved quantities

$$e \equiv -\vec{\xi} \cdot \vec{u} \tag{C7}$$

$$l \equiv \vec{\eta} \cdot \vec{u} \tag{C8}$$

with e and l being the conserved energy per unit rest mass and conserved angular momentum per unit rest mass respectively. $\vec{u}$ is the four-velocity.

From Eqs. (C7) and (C8) and using $u^{\tilde{r}} = 0$

$$e = -g_{vv}u^v - g_{v\tilde{\phi}'}u^{\tilde{\phi}'} \tag{C9}$$

$$l = g_{\tilde{\phi}'v}u^v + g_{\tilde{\phi}'\tilde{\phi}'}u^{\tilde{\phi}'}. \tag{C10}$$

From Eqs. (C9) and (C10)

$$u^v \equiv \frac{dv}{d\tau} = \frac{1}{\tilde{r}^2 - 2M\tilde{r} + a^2}[(\tilde{r}^2 + a^2 + \frac{2Ma^2}{\tilde{r}})e - \frac{2Ma}{\tilde{r}}l] \tag{C11}$$

$$u^{\tilde{\phi}'} \equiv \frac{d\tilde{\phi}'}{d\tau} = \frac{1}{\tilde{r}^2 - 2m\tilde{r} + a^2}[(1 - \frac{2M}{\tilde{r}})l + \frac{2Ma}{\tilde{r}}e]. \tag{C12}$$

$\Omega_{\tilde{\phi}'}$ is defined as

$$\Omega_{\tilde{\phi}'} \equiv \frac{d\tilde{\phi}'/d\tau}{dv/d\tau} = \frac{(1 - \frac{2M}{\tilde{r}})l/e + \frac{2Ma}{\tilde{r}}}{(\tilde{r}^2 + a^2 + \frac{2Ma^2}{\tilde{r}}) - \frac{2Ma}{\tilde{r}}l/e}. \tag{C13}$$

We need to substitute for l/e in Eq. (C13). Heading for that we can make use of the normalization condition

$$\vec{u} \cdot \vec{u} = -1, \tag{C14}$$

to find

$$\frac{e^2 - 1}{2} = \frac{1}{2}\frac{d\tilde{r}}{dt\tau} + [-\frac{M}{\tilde{r}} + \frac{l^2 - a^2(e^2 - 1)}{2\tilde{r}^2} - \frac{M(l - ae)^2}{\tilde{r}^3}]. \tag{C15}$$

Based on Eq. (C15), one can define the effective potential

$$V_{eff} = -\frac{M}{\tilde{r}} + \frac{l^2 - a^2(e^2-1)}{2\tilde{r}^2} - \frac{M(l-ae)^2}{\tilde{r}^3}. \tag{C16}$$

For a circular orbit of radius $\tilde{r}_0$, the effective potential has a minimum at $\tilde{r}_0$

$$\frac{\vartheta V_{eff}}{\vartheta \tilde{r}}(\tilde{r}_0) = 0 \tag{C17}$$

and also from Eq. (C15)

$$V_{eff}(\tilde{r}_0) = \frac{e^2-1}{2}. \tag{C18}$$

From Eqs. (C17) and (C18) one can solve for l/e: start from Eq. (C17)

$$\frac{\vartheta V_{eff}}{\vartheta \tilde{r}} = 0 \Rightarrow$$

$$\tilde{r} = \frac{-a^2(e^2-1) + l^2 + \sqrt{(a^2 - a^2e^2 + l^2)^2 - 12(l-ae)^2M^2}}{2M}. \tag{C19}$$

Now, from Eqs. (C18) and (C19) solve for l/e

$$\frac{l}{e} = \frac{-\tilde{r}^{3/2}(a^2 + \tilde{r}(\tilde{r}-2M)) + aM^{1/2}(a^2 + \tilde{r}(3\tilde{r}-4M))}{M^{1/2}(a^2M - \tilde{r}(\tilde{r}-2M)^2}. \tag{C20}$$

Substituting Eq. (C20) in Eq. (C13) will give

$$\Omega_{\tilde{\phi}'} = \pm\frac{M^{1/2}}{\tilde{r}^{3/2} \pm aM^{1/2}} \tag{C21}$$

with the upper and lower signs corresponding to co-rotating and counter-rotating orbits.

REFERENCES

Abbott, B., et al. 2006, Phys. Rev. D, 73, 062001

Apostolatos, T. A. 1995, Phys. Rev. D, 52, 605

Arun, K. G. 2006, Phys. Rev. D, 74, 024025

Baker, J.G., McWilliams, S. T., van Meter, J. R., Centrella, J., Choi, D., Kelly, B. J., & Koppitz, M. 2006, (gr-qc/0612117)

Barthelmy, S. D., et al. 2005, Nature, 438, 994

Belczynski, K., Taam, R. E., Kalogera, V., Rasio, F. A., & Bulik, T. 2007, (astro-ph/0612032)

Bogdanovic, T., Eracleous, M., Mahadevan, S., Sirgudsson, S., & Laguna, P. 2004, ApJ, 610, 707

Boyer, R.H., & Lindquist, R.W. 1967, J. of Math. Phys., 8, 265

Buonanno, A., Cook, G., & Pretorius, F. 2007 (gr-qc/0610122)

Burbidge, G. R., Burbidge, W. A., Fowler, W. A., & Hoyle, F. 1957, Rev. Mod. Phys., 29, 547

Burgay, M., DAmico, N., Possenti, A., et al. 2003, Nature, 426, 531

Burrows, D., et al. 2006, ApJ, 653, 468

Cameron, A. G. W. 1957, Pub. Astr. Soc. Pacific, 69, 201

Chandrasekhar, S. 1983, The Mathematical Theory of Black Holes, Oxford University Press

Dai, Z. G., Wang, X. Y., Wu, X. F., & Zhang, B. 2006, Science, 311, 1127

Faber, J. A., & Rasio, F. A. 2000, Phys. Rev. D 62, 064012

Faber, J. A., Rasio, F. A., & Manor, J. B. 2000, Phys. Rev. D, 63, 044012

Faber, J. A., & Rasio, F. A. 2002, Phys. Rev. D, 65, 084042

Faber, J.A., Grandclement, F., Rasio, F. A., & Taniguchi, K. 2002, Phys. Rev. Lett., 89, 231102

Faber, J. A., Baumgarte, T. W., Shapiro, S. L., & Taniguchi, K. 2006, ApJ, 641, L93

Faber, J. A., Baumgarte, T. W., Shapiro, S. L., Taniguchi, K., & Rasio, F. A. 2006, Phys. Rev. D, 73, 024012

Fox, D. B., et al. 2005, Nature, 437, 845

Frail, D., et al. 2001, ApJ, 562, L55

Fryer, C. L., Rockefeller, G., & Warren, M. S. 2006, ApJ, 643, 292

Galama, T. J., et al. 1998, Nature, 395, 670

Gehrels, N., et al. 2005, Nature, 437, 851

Gehrels, N., et al. 2006, Nature, 444, 1044

Grandclement, F., Kalogera, V., & Vecchio, A. 2003, Phys. Rev. D, 67, 042003

Grupe, D., et al. 2006, ApJ, 653, 462

Jaikumar, P., Meyer, B. S., Otsuki, K., & Ouyed, R. 2006, arXiv nucl-th/0610013 v1

Janka, H. T., Eberl, T., Ruffert, M., & Fryer, C. L. 1999, ApJ, 527, L39

Heitmann, K., Ricker, P. M., Warren, M. S., & Habib, S. 2005, ApJ, 160, 28

Hjorth, J., et al. 2003, Nature, 423, 847

Hartle, J. B. 2003, Gravity-An Introduction to Einstein's General Relativity,Addison Wesley

Hughes, S. 2000, Phys. Rev. D 61, 084004

Kalogera, V. 2000, ApJ, 541, 319

Kerr, R. P. 1963, Phys. Rev. Letters 11, 273

Kim, C., Kalogera, V., & Lorimer, D. R. 2003, ApJ, 584, 985

Kim, C., Kalogera, V., & Lorimer, D. R. 2006, (astro-ph/0608280)

Kluzniak, W., & Lee, W. H. 1998, ApJ, 494, L53

Kluzniak, W., & Lee, W. H. 2002, MNRAS, 335, L29

Kobayashi, S., Laguna, P., Phinney, E. S., & Mészáros, P. 2004, ApJ, 615, 855

Kouveliotou, C., et al. 1993, ApJ, 541, L101

Laguna, P., Miller, W. A. , & Zurek, W. H. 1993a, ApJ, 404 , L678

Laguna, P., Miller W. A., & Zurek, W. H. 1994, Mem. S.A.It. 65 1129L

Lai, D., Rasio, F. A., & Shapiro, S. L. 1994, ApJ, 437, 742

Lattimer, J., & Schramm, D. N. 1974, ApJ, 192, L145

Lattimer, J., & Schramm, D. N. 1976, ApJ, 210, 549

Lee, W. H., & Kluzniak, W. 1995, Acta Astronomica 45, 705

Lee, W. H., & Kluzniak, W. 1999, ApJ, 526, 178

Lee, W. H., & Kluzniak, W. 1999, MNRAS, 308, 780

Lee, W. H., Kluzniak, W., & Nix, J. 2001, Acta Astronomica 51, 331

Lipunov, V. M., Postnov, K. A., & Prokhorov, M. E. 1997, MNRAS, 288, 245L

MacFadyen, A. I., & Woosley, S. E. 1999, ApJ, 524, 262

Mészáros, P. 2006, Rep.of Prog. in Phys, 69, 2259

Mészáros, P., Rees, M. J.,& Wijers, R.A.M.J. 1999, New Astronomy, 4, 303

Misner, C. W., Thorne, K. S., & Wheeler, J. A. 1973, Gravitation, (Freeman, San Fransisco, 1973), chap.33

Monfardini, A., et al. 2006, ApJ, 648, 1125

Nakar, E. 2007, Physics Reports - Bethe Centennial Volume, in press (astro-ph/0701248)

Nelemans, G., Yungelson, L. R., & Portegies Zwart, S. F. 2001, A&A, 375, 890

O'Shaughnessy, R., Kim, C., Fragos, T., Kalogera, V., & Belczynski, K. 2005, ApJ, 633, 1076

O'Shaughnessy, R., Kim, C., Kalogera, V., & Belczynski, K. 2006, (astro-ph/0610076)

Perna, R., & Belczynski, K. 2002, ApJ, 570, 252

Perna, R., Armitage, P. J., & Zhang, B. 2006, ApJ, 636, L29

Pian, E., et al. 2006, Nature, 442, 1011

Piran, T. 2004, Reviews of Mod. Phys., 76, 1143

Poisson, E., & Will, C. M. 1995, Phys.Rev. D, 52, 848

Poisson, E. 2004, A Relativist's toolkit, (Cambridge: University Press)

Proga, D., & Zhang, B. 2006, MNRAS, 370, L61

Rasio, F. A., & Shapiro, S. L. 1995, ApJ, 438, 887

Rosswog, S., Speith, R., & Wynn, G. A. 2004, MNRS, 351, 1121

Rosswog, S. 2005, ApJ, 634, 1202

Shibata, M., & Uryu, K. 2006a (astro-ph/0611522)

Shibata, M., & Uryu, K. 2006b, Phys.Rev. D, 74, 121503

Soderberg, A., et al. 2006, ApJ, 650, 261

Thorsett, S. E., & Chakrabarty, D. 1999, ApJ, 512, 288

Vallisneri, M. 2002, Phys. Rev. Lett., 84, 3519

Vallisneri, M. 2002, in The Ninth Marcel Grossmann Meeting, ed. V. G. Gurzadyan, R. T. Jantzen, R. Ruffini , (Singapore: World Scientific Publishing), 1672V

Villasenor, J. S., et al. 2005, Nature, 437, 855

von Neumann, J., & Rithmyer R. D. 1950, J. Appl. Phys., 21, 232

Warren, M. S., & Salmon, J. K. 1991, BAAS, 23.1345W

Wiggins, P., & Lai, D. 2000, ApJ, 532, 530

Wilkins, D. C., 1972, Phys. Rev. D, 5, 814

Woosley, S. E., & Bloom, J. S. 2006, Ann. Rev. Astron. Astrophys., 44, 507

Zhang, B., et al. 2006, ApJ, 642, 354

Table 1. Runs and their results for simulations of equatorial mergers

Run	**E1**	**E2**	**E3**	**E4**	**E5**	**E6**	**E7**	**E8**	**E9**	**E10**
a/M	0.99	0.95	0.9	0.8	0.75	0.6	0.5	0.2	0.1	0
Total NS mass outside r_+	33 %	32%	26%	4%	1%	0%	0%	0%	0%	0%
Bound NS mass outside r_+	2.5%	2%	0%	0%	0%	0%	0%	0%	0%	0%

Table 2. Initial conditions and results for the simulations of inclined BH–NS mergers

Run	**I1**	**I2**	**I3**	**I4**	**I5**
a/M	0.99	0.99	0.99	0.99	0.99
$\mathbf{r_0(M)}$	12	11.5	12	13	10
inclination angle (^{o})	30	45	70	90	180
Total NS mass outside r_+	37%	25%	0%	0%	0%
Bound NS mass outside r_+	6%	0%	0%	0%	0%

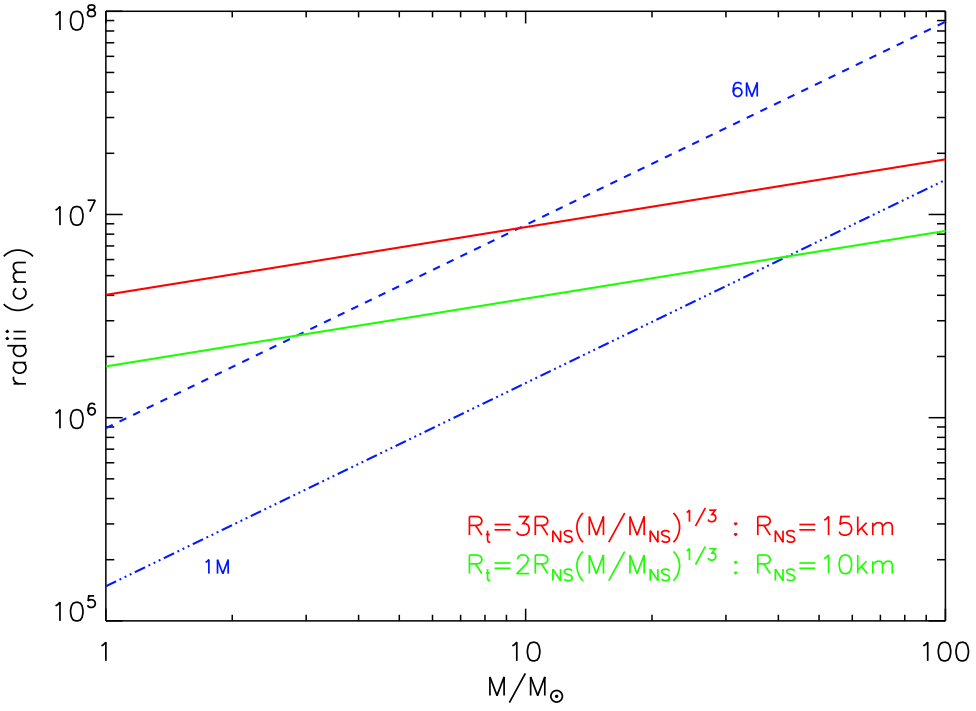

Fig. 1.— Tidal disruption limits for a $1.4\,M_\odot$ NS in circular orbit around a BH of mass M. The radius of the ISCO (in geometrized units) is also shown for the Schwarzschild (dashed line) and maximally co-rotating Kerr cases (dash-dotted line). The two solid lines bracket the tidal limit for NS with different spins and radii (Wiggins & Lai 2000; Lai et al. 1994). Orbits are assumed to be in the equatorial plane and prograde.

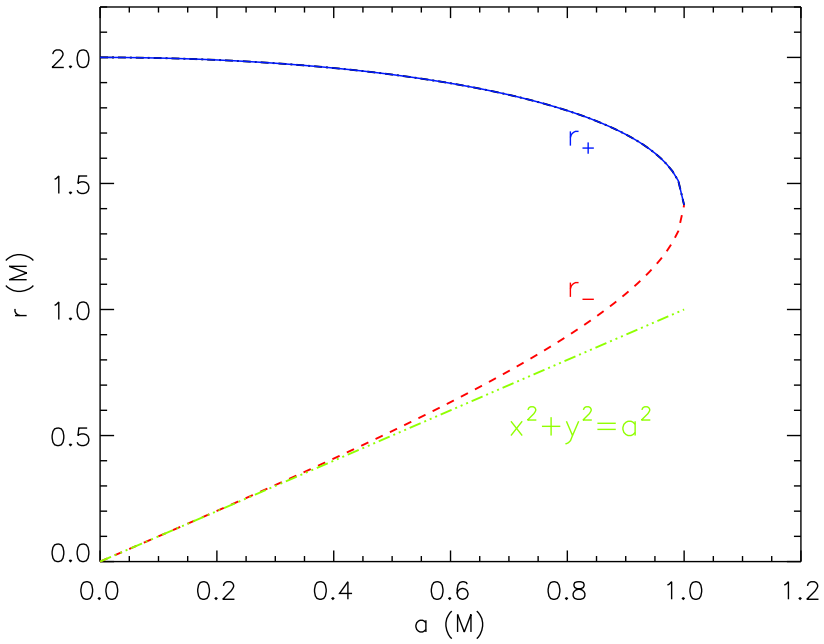

Fig. 2.— The future (solid blue line) and past (dashed red line) horizons of a BH for various values of the BH's angular momentum a. The third (dash-dotted green) line represents the ring (curvature) singularity of the K-S metric, that exists only on the equatorial plane.

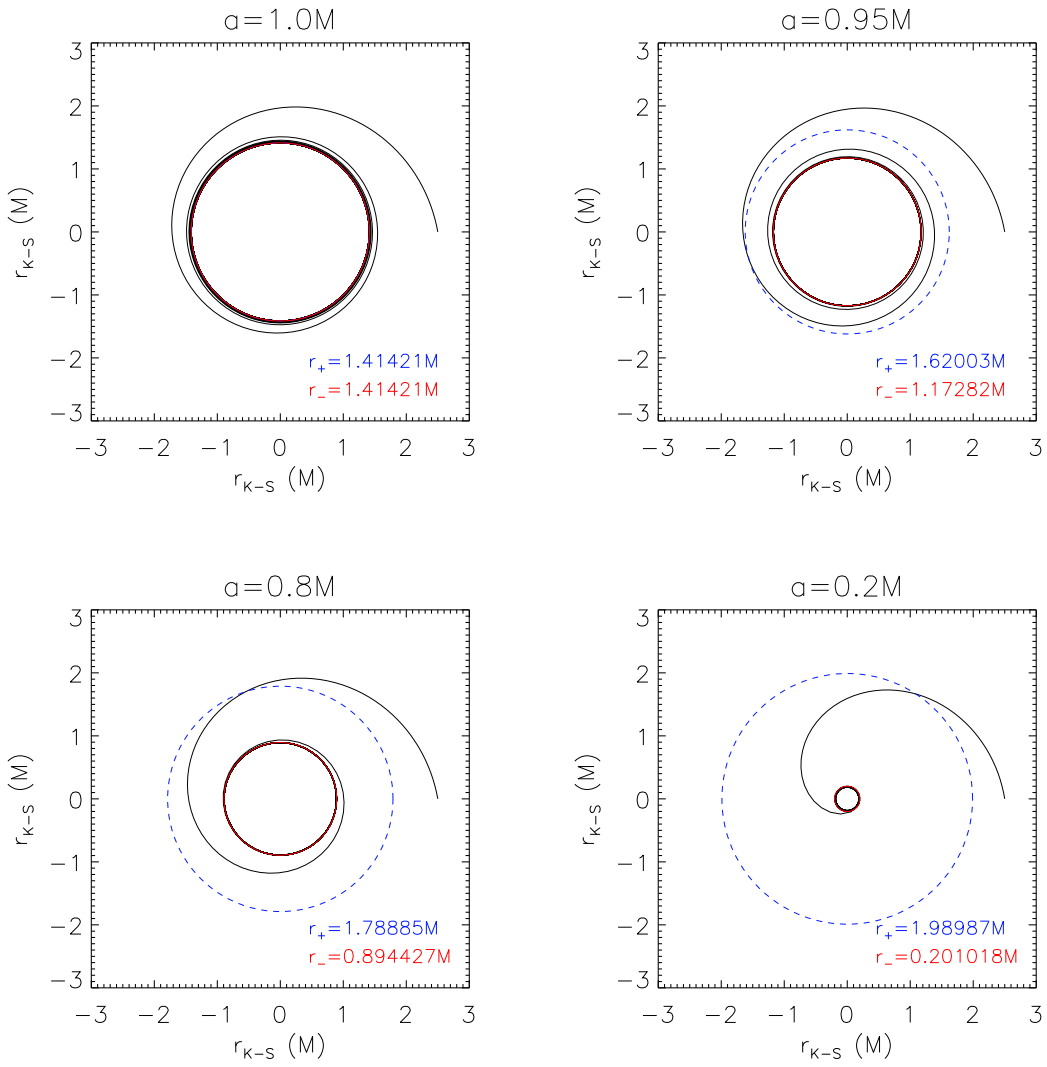

Fig. 3.— A 'horizon-trapped' orbit for different values of a. The initial conditions for the particle are fixed and only a is varied in the four orbits.The red circles represent the two horizons. It is clear that the particle successfully crosses the outer horizon and ends being trapped in the inner horizon, except for the $a = M$ case where the two horizons coincide.

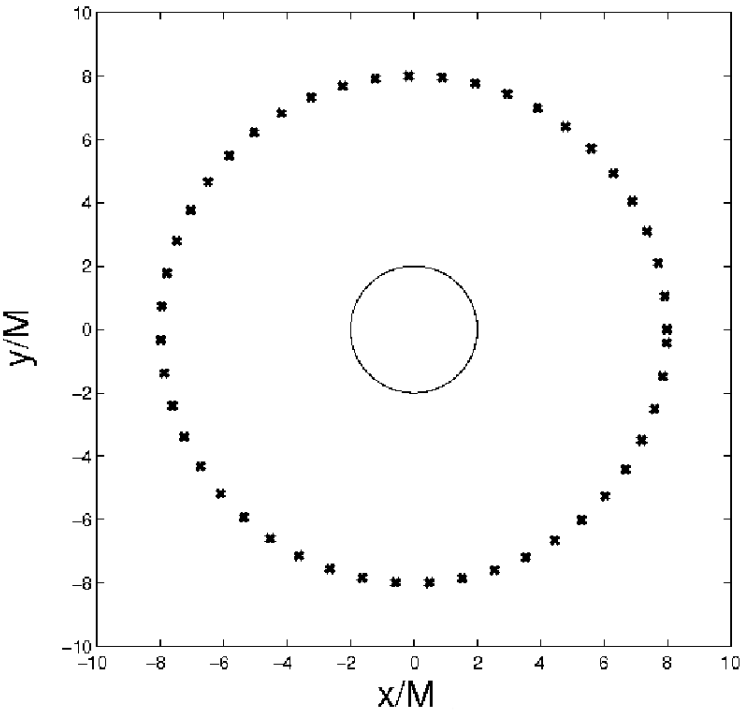

Fig. 4.— Test calculation for a WD orbiting a much more massive BH at $r = 8\,\mathrm{M}$. The mass ratio in this case is $q \simeq 4 \times 10^5$. The constant radius of this circular orbit is maintained by our code to within better than 10^{-3} over one full period. Here each cross indicates the position of the WD (center of mass of all SPH particles) at a different time along the orbit (counter-clockwise).

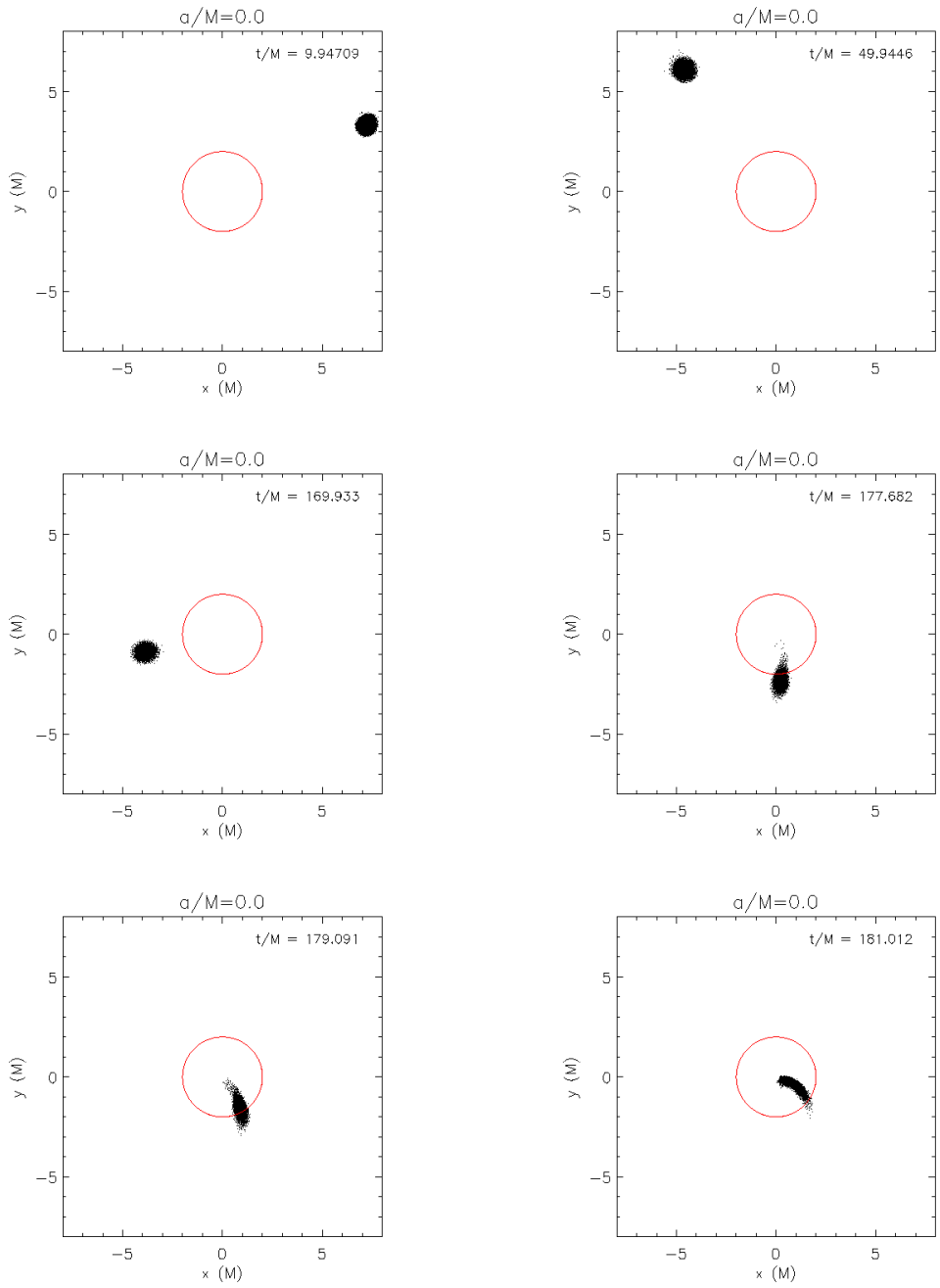

Fig. 5.— Sequence of six snapshots of a non-spinning BH–NS merger simulation (equatorial projection.) The $1.4\,M_\odot$ NS gets completely disrupted by a non-rotating BH of mass $M = 15\,M_\odot$. The NS was initially placed outside the tidal limit ($r \simeq 8\,M$ for this NS of radius $R \simeq 15\,\mathrm{km}$ with a $\Gamma = 2$ polytropic EOS). The NS fluid is disappearing completely into the BH's horizon (at $r = 2M$, indicated by the red circle) at a timescale of $t/M = 180$ after the beginning of the simulation.

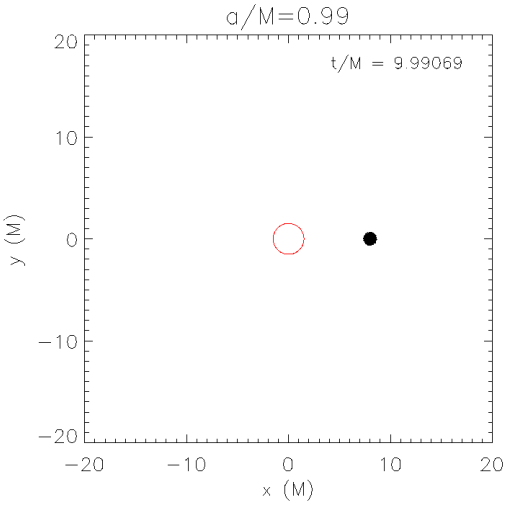
a/M=0.99
t/M = 9.99069
y (M)
x (M)

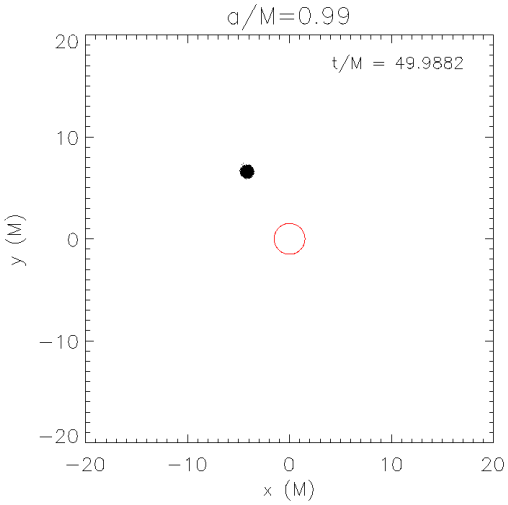
a/M=0.99
t/M = 49.9882
y (M)
x (M)

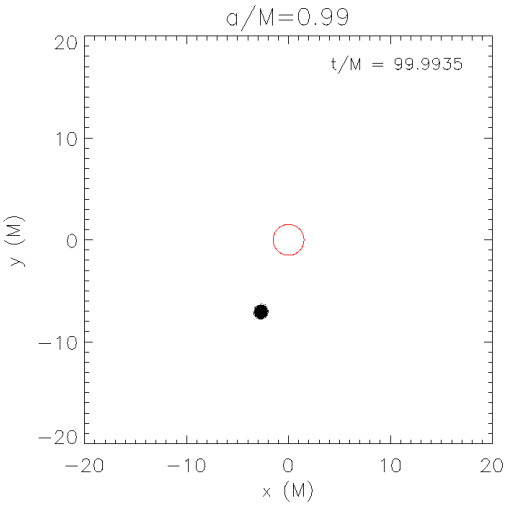
a/M=0.99
t/M = 99.9935
y (M)
x (M)

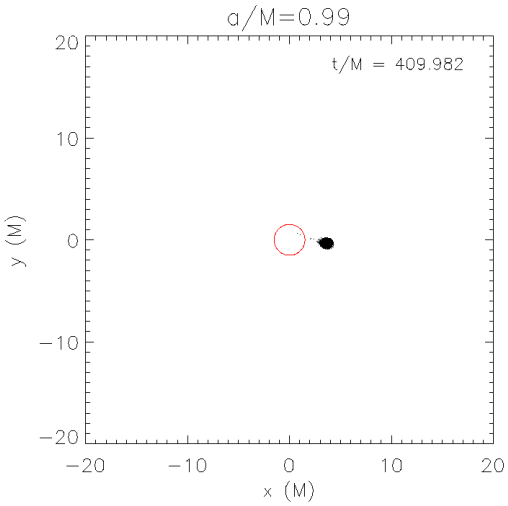
a/M=0.99
t/M = 409.982
y (M)
x (M)

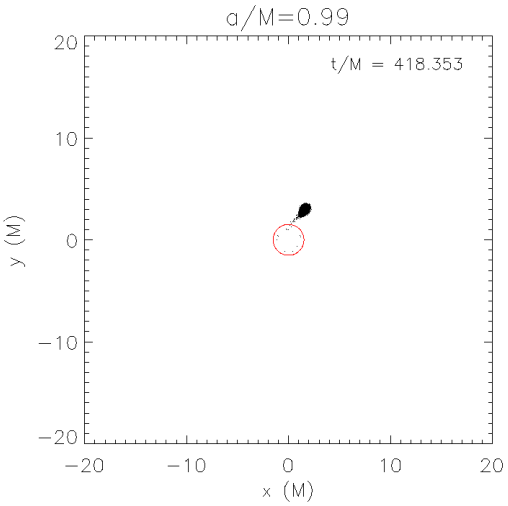
a/M=0.99
t/M = 418.353
y (M)
x (M)

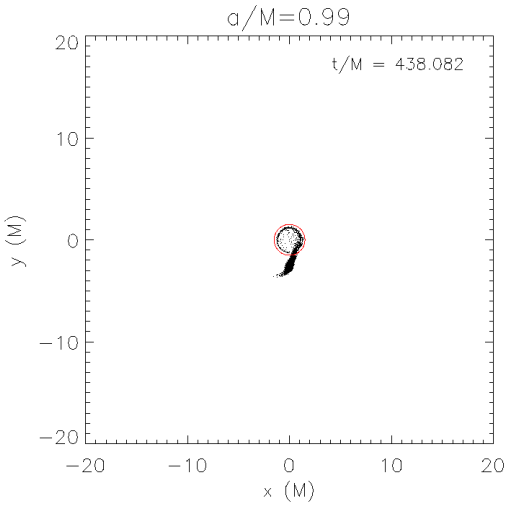
a/M=0.99
t/M = 438.082
y (M)
x (M)

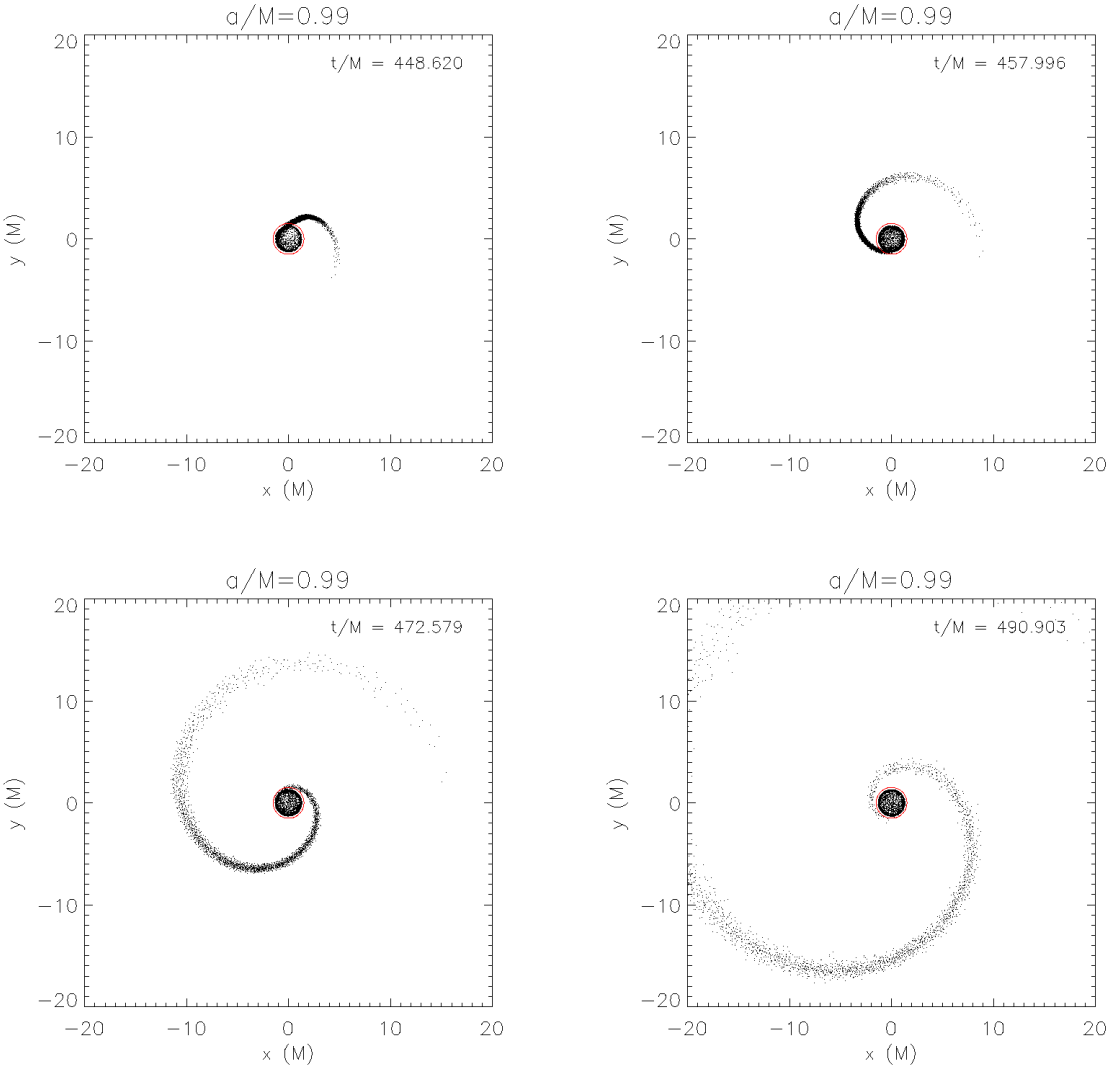

Fig. 6.— Same as in Fig. 5 but for a rotating BH with $a/M = 0.99$. Except for the mass getting lost inside the BH's horizon, there's a tail of expanding material forming. By the end of the simulation ($t/M \sim 550$) the infall of material stops completely and 33% of the NS's mass resides outside the horizon, with $\sim 30\%$ corresponding to unbound ejected material and the rest of it to bound disk-forming mass.

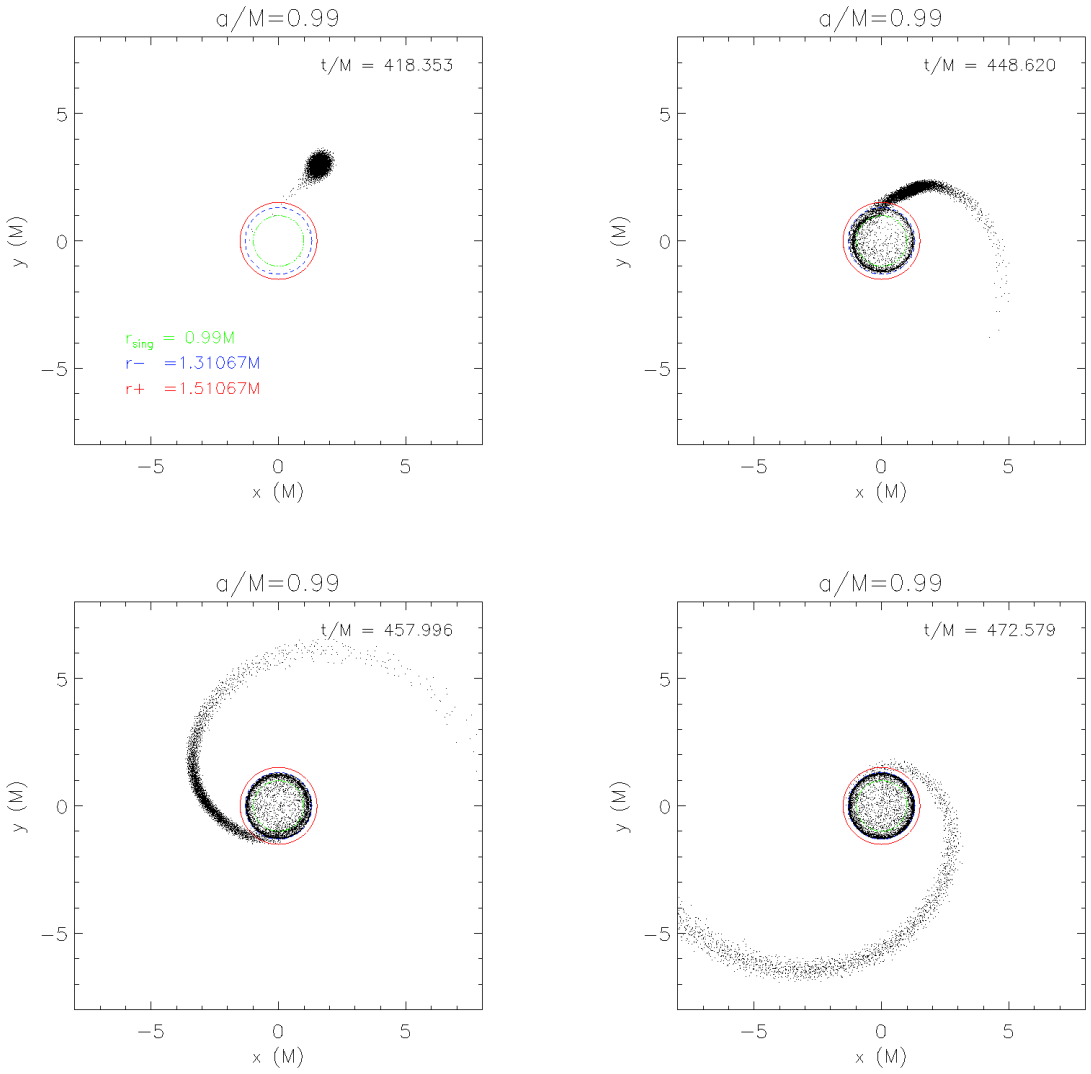

Fig. 7.— A close up view on the central part of four of the snapshots in Fig. 6. The three colored circles represent in K-S coordinates the BH's future horizon r_+ (blue), the past horizon r_-(red) and the ring singularity at $r = a$ (green). Here it is illustrated what was mentioned at paragraph §2.1.1: the metric's singularity at the inner (past) horizon translates to the 'illusive' formation of a ring on the equatorial plane with radius $r = r_-$.

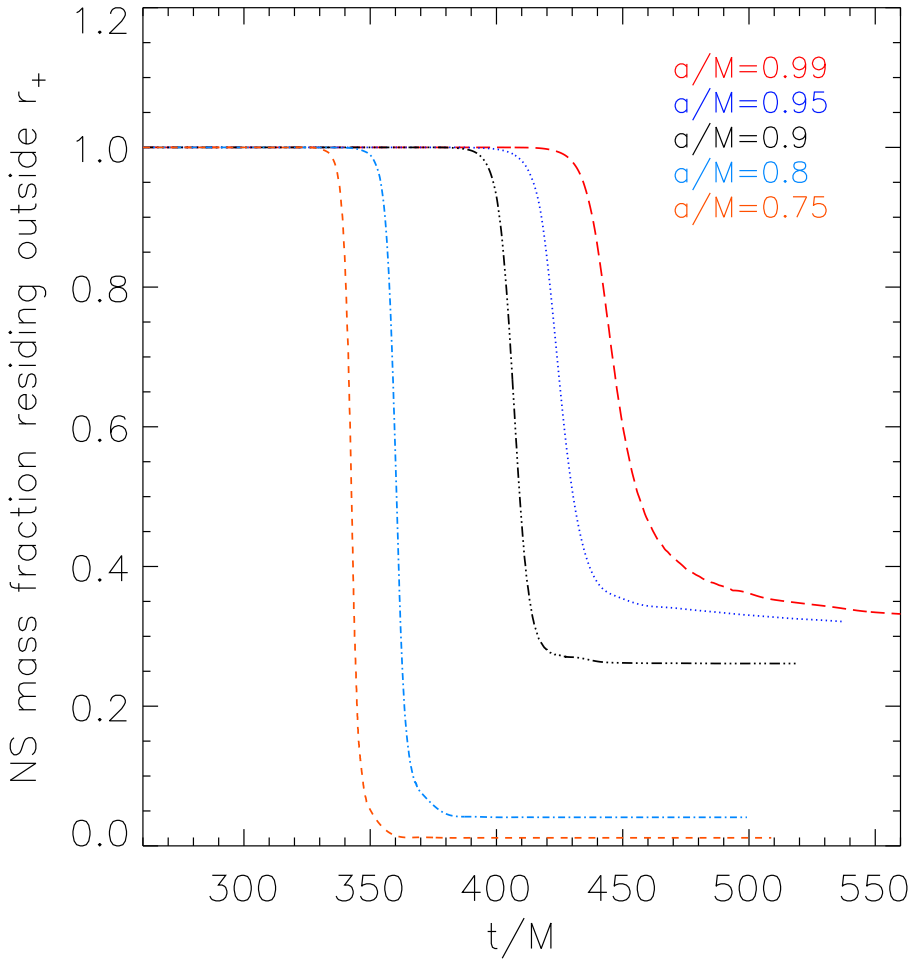

Fig. 8.— Fraction of the NS's initial mass that resides outside the BH's future horizon as a function of time, for five different values of the BH's angular momentum a/M ($0.75 \leq a/M \leq 0.99$). The survival of NS material outside the BH's horizon depends strongly on the BH's angular momentum. As a/M decreases the fraction of surviving mass decreases aswell and the merger becomes completely catastrophical for the NS for values $a/M \lesssim 0.7$. Also the accretion of material into the BH's horizon starts earlier as the BH's angular momentum decreases; something to be expected as the BH's horizon is moving further away from the BH with decreasing a/M.

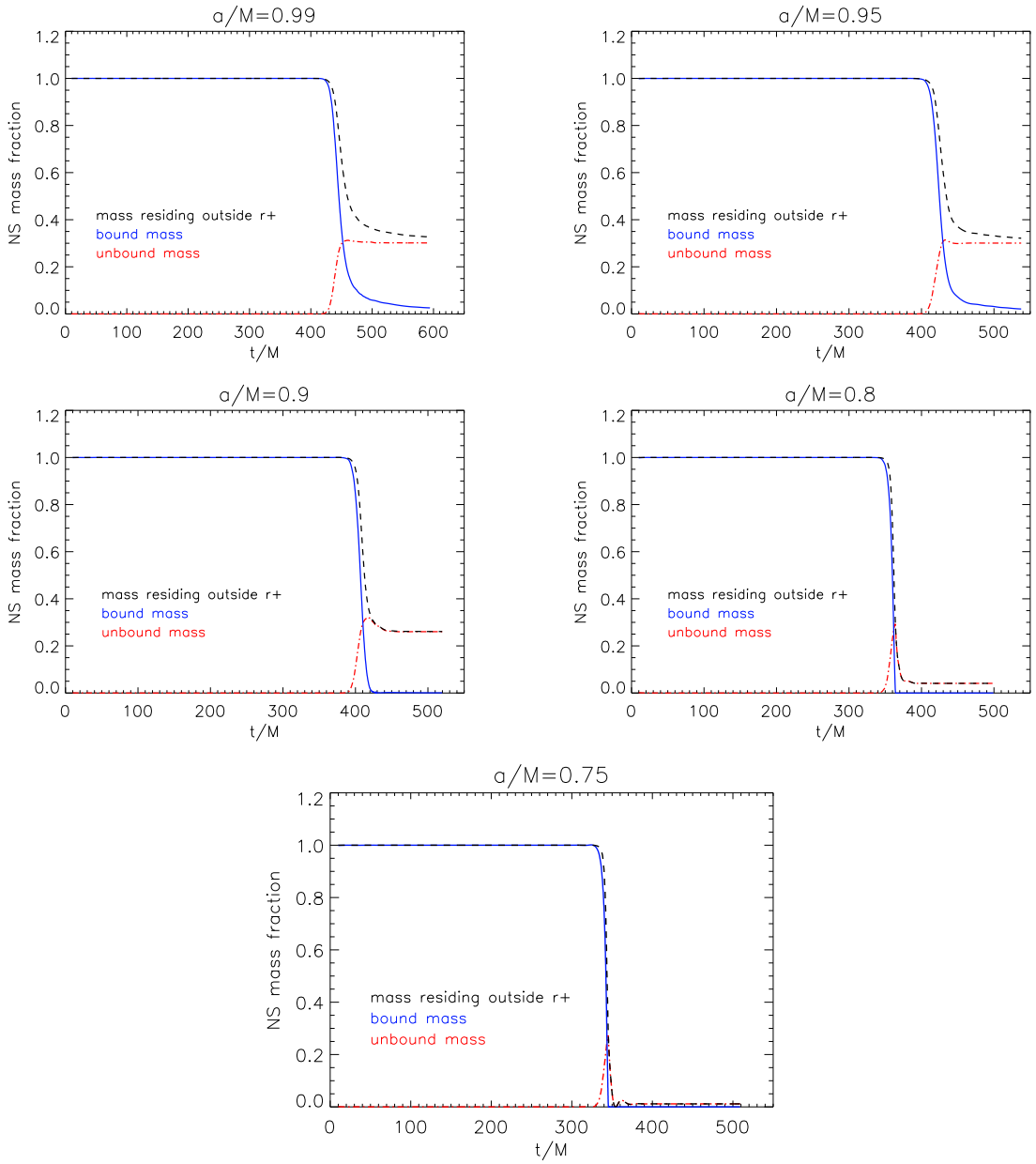

Fig. 9.— Fractions of total (black line), bound (blue line) and unbound (red line) material of the NS's initial mass as a function of time for five different simulations, corresponding to five different values of a/M (runs E1-E5). For values of $a/M < 0.95$ the percentage of surviving bound material drops to unresolvable by our code levels.

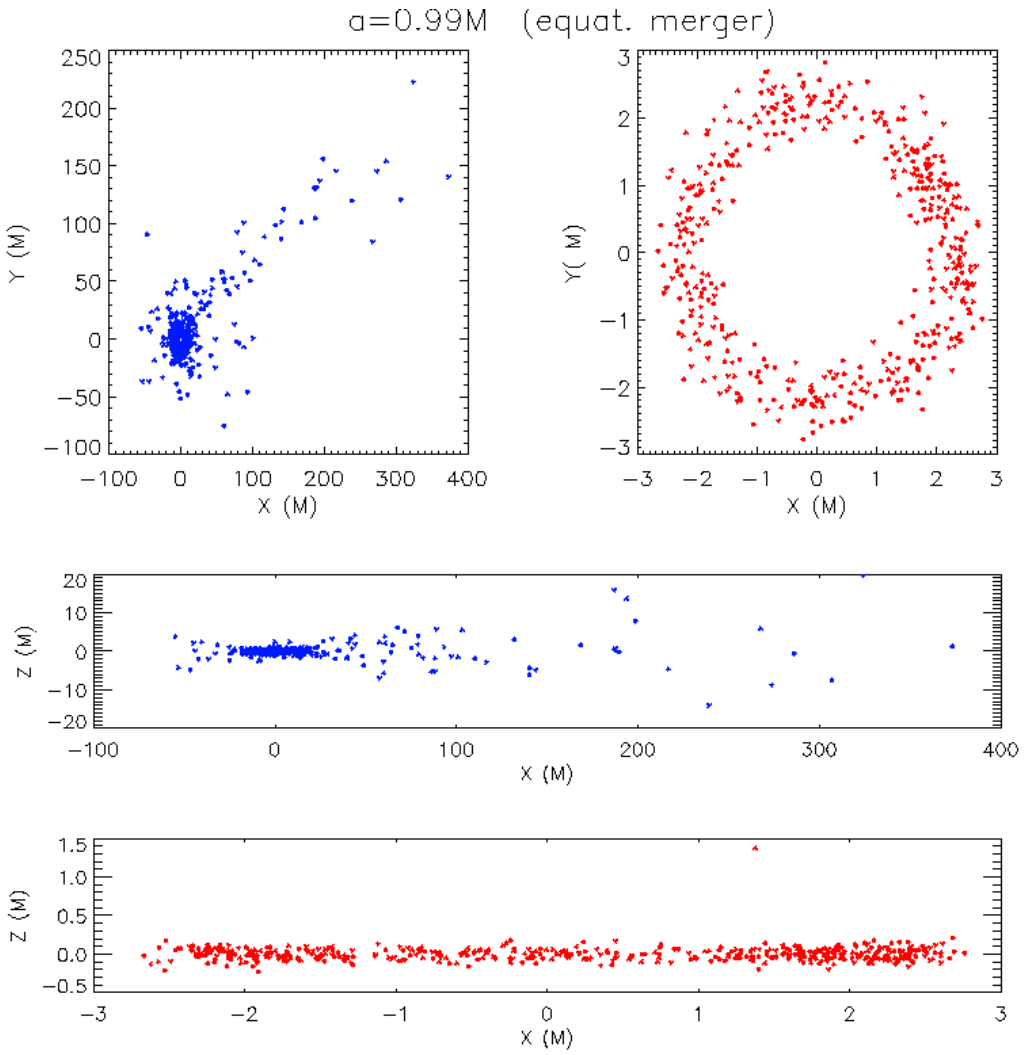

Fig. 10.— Spatial distribution of the apocenters (blue) and the pericenters (red) for the disk-forming SPH particles of the $a = 0.99M$ equatorial merger (Run E1). The upper left (right) and middle (bottom) panels correspond to the x-y and x-z plane projections for the apocenters (pericenters) respectively. The total mass of the disk is 2.5% of the initial NS mass. The mean pericenter value (inner radius of the disk) is $r_{peri} \sim 2.5M$ and the mean apocenter (outer radius of the disk) is $r_{apo} \sim 30M$.

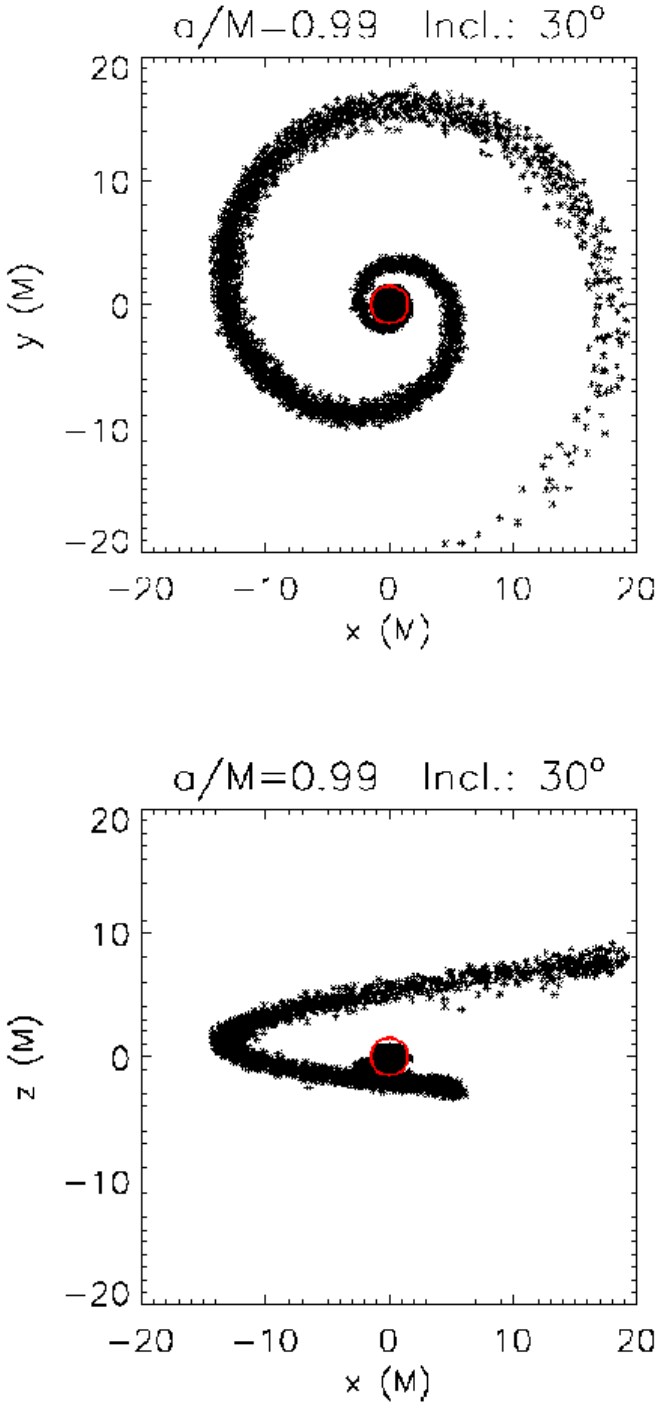

Fig. 11.— Snapshot of Run I1 (up) and its x-z projection (down) towards the end of the simulation.The red circle represents the BH's outer horizon. The material that survives the merger forms an expanding helix. For this particular run 30% of the initial NS's mass gets dynamically ejected and 6% remains bound, forming a stable torus outside the BH's horizon.

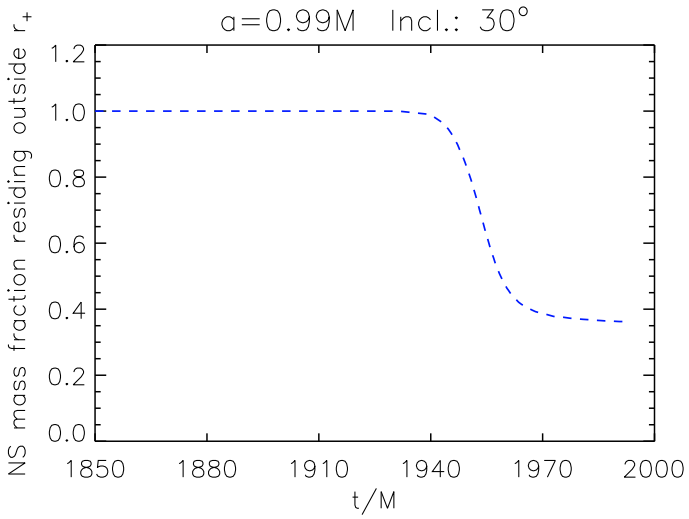

Fig. 12.— Fraction of the NS's mass that resides outside the BH's future horizon for Run I1. At time $t/M = 1950$ after the beginning of the simulation, the surviving material stabilizes at $\sim 37\%$. 31% corresponds to unbound escaping mass, while 6% stays bound and forms a torus around the BH's horizon.

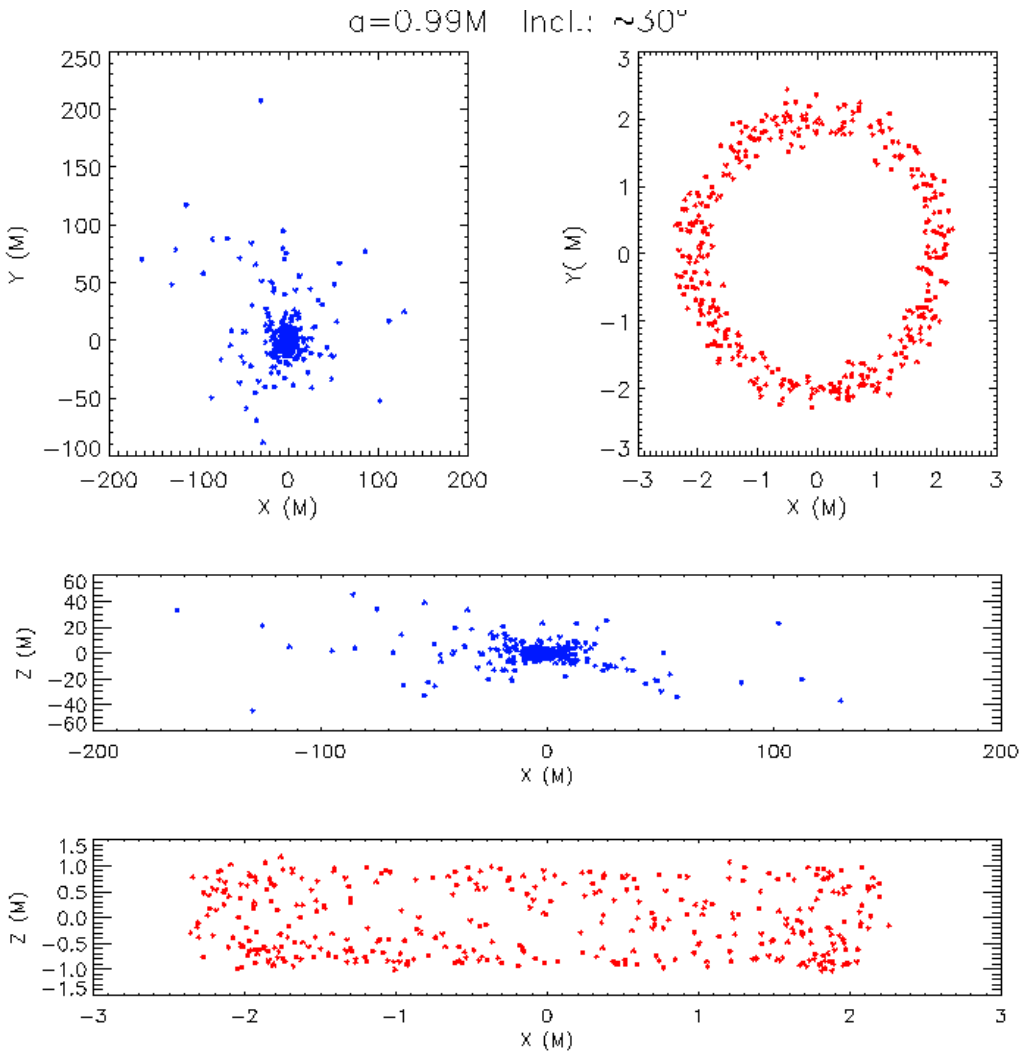

Fig. 13.— Spatial distribution of the apocenters (blue) and the pericenters (red) for the bound SPH particles of Run I1. It is noticeable that in inclined mergers the bound mass forms a torus rather than a disk, as it is the case for the equatorial mergers (Fig. 10). The upper left (right) and middle (bottom) panels correspond to the x-y and x-z plane projections for the apocenters (pericenters) respectively. The total mass of the torus is 6% of the initial NS mass. The mean pericenter value (inner radius of the torus) is $r_{peri} \sim 2.0M$ and the mean apocenter (outer radius of the torus) is $r_{apo} \sim 25M$.

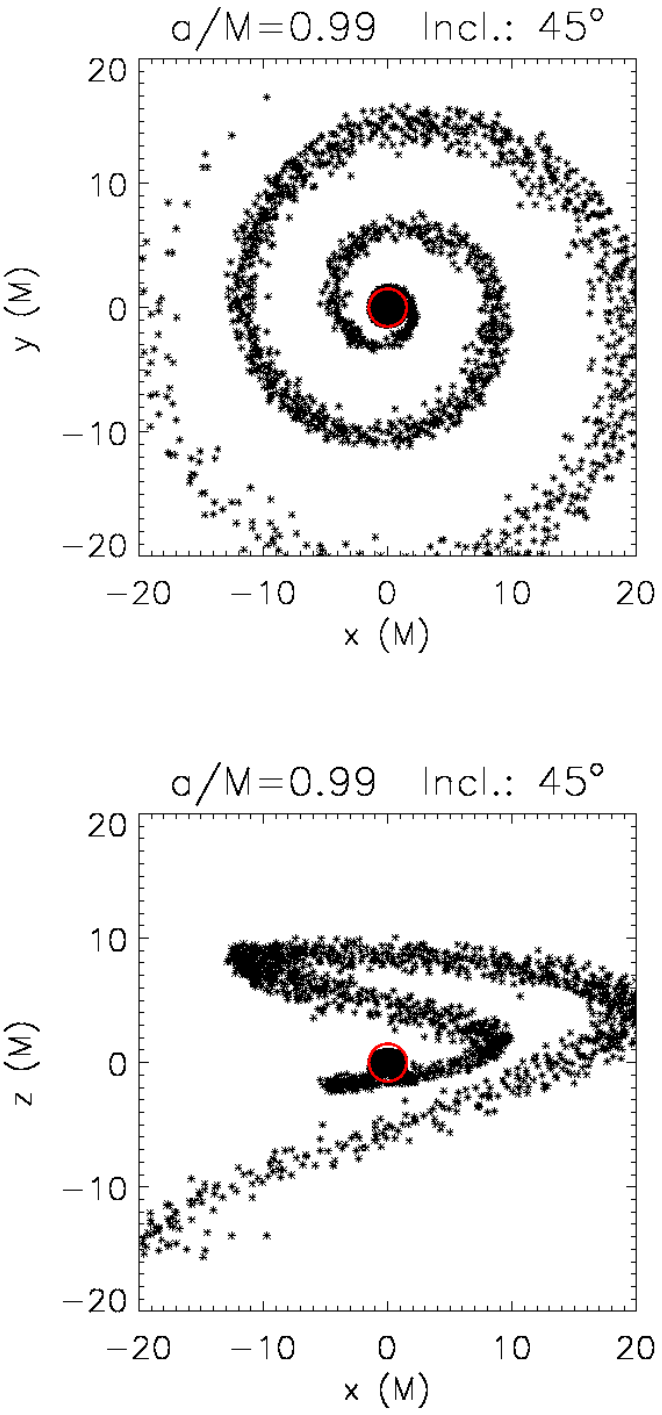

Fig. 14.— Snapshot of Run I2 (up) and its x-z projection (down) towards the end of the simulation.The red circle represents the BH's outer horizon. By the end of the simulation an outwards expanding helix has formed, ejecting 25% of the initial NS's mass away from the BH. The fraction of surviving bound material was too small to be resolved in this calculation.

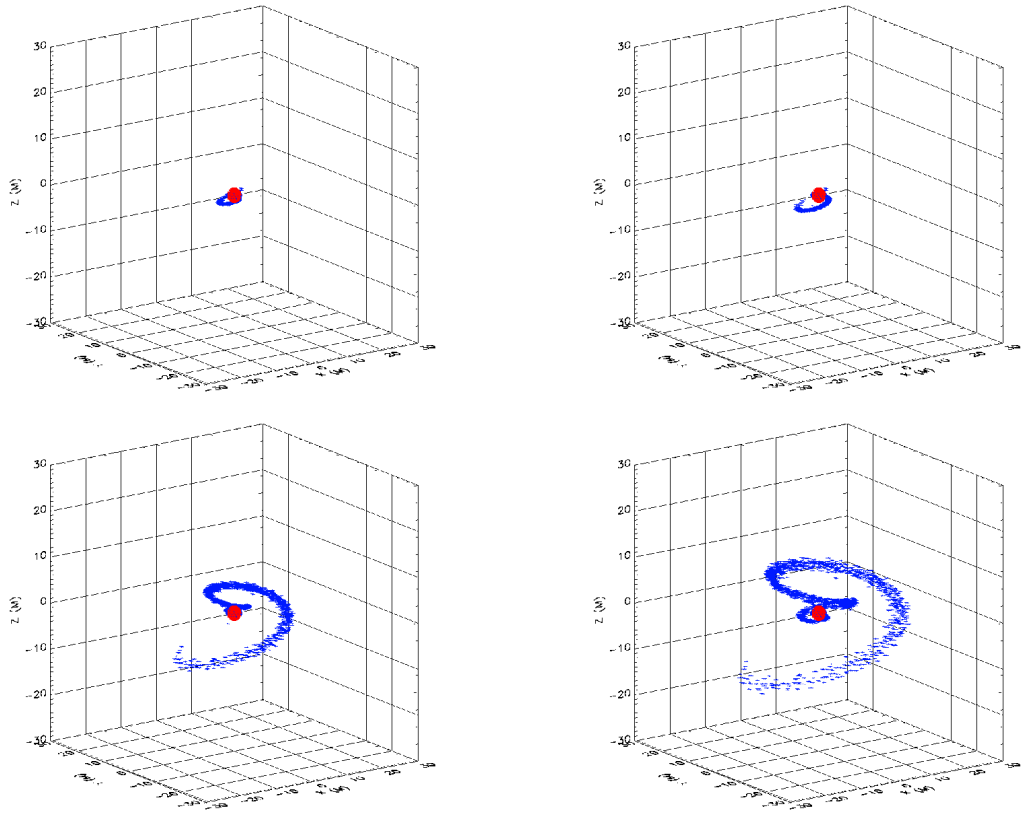

Fig. 15.— Four 3-D snapshots of Run I2 towards the end of the simulation. The NS has already been disrupted and starts accreting material into the BH's horizon. An expanding helix of unbound material forms at the same time, resulting to the ejection of 25% of the NS mass.

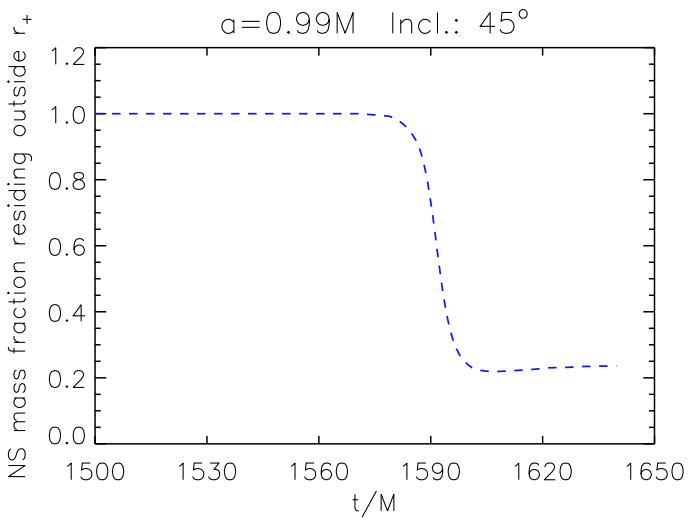

Fig. 16.— Fraction of the NS's mass that resides outside the BH's future horizon for Run I2. At time $t/M = 1600$ after the beginning of the simulation, the surviving material stabilizes at 25% almost all of which is unbound and therefore escaping outwards.

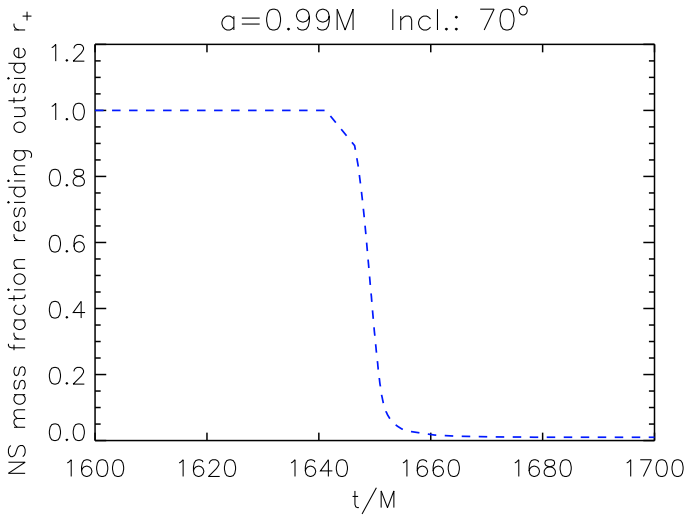

Fig. 17.— Fraction of the NS's mass that resides outside the BH's future horizon for Run I3. At tine $t/M = 1640$ after the beginning of the simulation, the whole NS mass has crossed the BH's outer horizon.